



Judith Lammer, BSc

Experimental Determination of the Solid Angle of Energy-Dispersive X-ray Detectors

MASTER'S THESIS

to achieve the university degree of

Diplom-Ingenieurin

Master's degree programme: Technical Physics

submitted to

Graz University of Technology

Supervisor

Ao. Univ.-Prof. Dipl.-Ing. Dr. techn. Werner Grogger

Institute of Electron Microscopy and Nanoanalysis

AFFIDAVIT

I declare that I have authored this thesis independently, that I have not used other than the declared sources/resources, and that I have explicitly indicated all material which has been quoted either literally or by content from the sources used. The text document uploaded to TUGRAZonline is identical to the present master's thesis.

Date

Signature

Kurzfassung

Ein limitierender instrumentenspezifischer Parameter in der energiedispersiven Röntgenspektrometrie (EDXS) ist die Größe des Raumwinkels des EDXS Detektors: Charakteristische Röntgenstrahlung wird in alle Raumrichtungen gleichverteilt emittiert, erfasst wird jedoch nur jener Teil innerhalb des Raumwinkels des Detektors. Ein größerer Raumwinkel führt zu einer Verbesserung des Sammelwirkungsgrads und der Sensitivität des Detektors. Geometrische Berechnungen des Raumwinkels sind schwer durchzuführen, weil sie auf der Kenntnis der Geometrie des Detektorsystems beruhen, die meist nur teilweise bekannt ist. In dieser Arbeit wird ein experimenteller Ansatz zu Messung des Raumwinkels vorgestellt, welcher eine bereits bestehende einfache Messmethode mit einem einzelnen Messstandard mit der ζ -factor Methode kombiniert. Diese Herangehensweise wurde verwendet, um die Raumwinkel zweier EDXS Detektoren an zwei verschiedenen Transmissionselektronenmikroskopen zu ermitteln.

Dieser Ansatz setzt vorhandene Werte für Ionisationsquerschnitte, Fluoreszenzausbeuten sowie relative Linienintensitäten voraus. Diesbezüglich wurde eine ausführliche Literatur- und Datenbankenrecherche durchgeführt. Des Weiteren werden ζ -Faktoren benötigt, welche für sechs Elemente (Al, Si, Ti, Ga, As, Sr) mit Hilfe der EDXS gemessen wurden. Die Verwendung von verschiedenen Elementen und fundierten Werten der Datenbanken erhöht die Genauigkeit dieser Messmethode und ermöglicht eine fundierte Bestimmung des Raumwinkels.

Abstract

A limiting parameter in energy-dispersive X-ray spectrometry (EDXS) in a transmission electron microscope (TEM) is the magnitude of the solid angle of the EDXS detector: characteristic X-rays are emitted; they are equally distributed into the whole space, but only a small part within the detector solid angle is detected. A larger solid angle results in a larger collection efficiency of X-rays and a higher sensitivity of the detector. A geometrical calculation of the solid angle is difficult since the detector geometry is not very well known. In this work an experimental approach to obtain the solid angle is presented combining an already existing straightforward measurement procedure with a single standard sample and the ζ -factor method. Furthermore it is used for the determination of the solid angles of two different EDXS detectors on two different TEMs.

This approach requires data for ionization cross sections, fluorescence yields and relative line intensity ratios, which is why an extensive research for literature and databases was performed. In addition ζ -factors were measured for six elements (Al, Si, Ti, Ga, As, Sr) via EDXS. The use of different elements and of state-of-the-art parameters enhances the accuracy of the procedure and enables us to determine the solid angle of our EDXS systems properly.

Acknowledgments

At this point I would like to acknowledge all people who made this work possible and supported me.

I want to thank my supervisor Werner Grogger for giving me the opportunity to write this master thesis, for his remarkable support and scientific guidance through my whole work. Moreover I express my gratitude to Johanna Kraxner for her tremendous encouragement, for spending her time measuring with me at the microscopes and giving me competent advice to bring my work to a successful completion.

I would also like to thank Margit Brunegger for purchasing even not obtainable literature for me and Sebastian Rauch for his accurate specimen preparation with the FIB. I also would like to acknowledge Martina Dienstleder, Christian Gspan, Daniel Knez, and Georg Haberfehlner for participating in rewarding discussions and giving me good advice.

Special thanks go to my office colleagues Stefanie Stückler and Franz Schmidt for having inspiring conversations about microscopy and English language in scientific writing. You sweetened my working days with your presence and a huge amount of cake every week.

A great thank you also goes to the whole FELMI-ZFE team. I wouldn't have wanted to miss the coffee and lunch breaks, beach volleyball games and parties.

Last but not least I want to thank my family and friends for your moral support, your patience and for being there for me every time I needed you.

Contents

1	Introduction	1
2	Fundamentals of Energy-Dispersive X-ray Spectrometry in Transmission Electron Microscopy	3
2.1	Generation of X-Rays	3
2.2	The Energy-Dispersive X-ray Spectrometer	6
2.3	Semiconductor Detectors	6
2.4	Detector Efficiency	8
2.5	The Solid Angle	9
2.6	Quantitative X-ray Analysis Using ζ -Factors	12
2.7	How to Determine the Solid Angle via ζ -Factors	14
3	Databases	15
3.1	Relative Line Intensity Ratios	15
3.1.1	Theoretical Calculation via Hartree-Slater and Hartree-Fock	16
3.1.2	Available Data from <i>MA-Table</i>	17
3.2	Fluorescence Yields	19
3.2.1	Calculating Fluorescence Yields from Transition Probabilities and Widths	20
3.2.2	The Database Livermore Evaluated Atomic Data Library (EADL) . . .	21
3.3	Ionization Cross Sections	23
3.3.1	Plane-Wave Born Approximation and Distorted-Wave Born Approximation	24
3.3.2	<i>NIST 164</i> Database	25
3.4	Comparing Values Used by Egerton et al. [24] to the New Databases	27
4	Experiments	29
4.1	Specimens	29
4.1.1	Choice of Samples	29
4.1.2	Specimen Preparation	30
4.2	Used TEM-EDXS Systems	31
4.3	Experimental Set-up	32
4.4	Acquisition of Required Data	33
4.4.1	Determining Peak Intensities of EDX Spectra	34
4.4.2	Thickness Determination with t/λ Measurements	37

4.5 ζ -Factor Determination	39
4.6 Solid Angle Determination	42
5 Conclusion	45
Bibliography	47

ATOMYRIADES

Nature, it seems, is the popular name
for milliards and milliards and milliards
of particles playing their infinite game
of billiards and billiards and billiards.

»Natur« ist, scheint's, bloß ein anderes Wort
für Milljarden, Milljarden, Milljarden
von Teilchen, die in einem fort
billjarden, billjarden, billjarden.

Piet Hein

CHAPTER 1

Introduction

Nanotechnology is an important field in science and industrial research for medicine, electronics, surface coating, energy generation, cosmetics, agriculture, and many other domains. So far, many applications have been developed, e.g. devices within nanometer scale, new material compounds and materials with modified surface characteristics. For all these applications it is essential to have analysis instruments resolving details down to the nanometer scale at one's disposal. One instrument (amongst many) that provides structural and chemical information about smallest areas is the transmission electron microscope (TEM). State-of-the-art TEMs are able to reach resolutions smaller than 100 pm. This means that high resolution images of crystals, lattice defects, grain boundaries, and even the detection of single atoms are possible. As already mentioned, not only imaging but also chemical analyses of materials is provided by a TEM. Two standard techniques are used for chemical analysis: electron energy loss spectroscopy (EELS) and energy-dispersive X-ray spectrometry (EDXS).

Electrons that hit the specimen may interact with the atoms in the sample and thereby loose energy. Inferences about the composition of the specimen can be made by examining the energy-loss of these electrons using EELS. If the incident electrons cause ionizations in the specimen, characteristic X-rays may be emitted by the ionized atoms. The chemical information carried by these X-rays is obtained via EDXS. EDXS has been used to analyze middle and heavy elements, whereas EELS has been preferentially used for light elements. Thanks to enhancements modern EDXS detectors allow already the detection down to beryllium. Moreover, EELS provides additional information concerning the electronic structure and chemical bonding.

EDXS is a suitable tool for quantitative analysis using either the Cliff-Lorimer technique or the newer ζ -factor method. The ζ -factor method has the advantages, that one can also use pure-element standards instead of multielement standards and that a mass thickness determination of specimens with simultaneous X-ray absorption correction is possible. A precondition for the reliability of quantification with the ζ -factor method is the correct determination of sensitivity factors (the so-called ζ -factors). They can either be measured using reference specimens or be theoretically evaluated.

The performance of an EDXS system is expressed in several parameters, which are specific to the used instrument. One of them describes the collection angle within which the EDXS is capable of detecting X-rays, which is called the detector solid angle. Characteristic X-rays are emitted equally and being distributed into the whole space (4π sr) but only a small part is detected. Typical values for solid angles EDXS detectors are around 0.1 sr, but at the present there are endeavours to enlarge the solid angle of EDXS detectors. A larger solid angle results in a larger collection efficiency of X-rays, i.e. an increase in detected X-rays. A determination of the detector solid angle can be done experimentally or via a geometrical calculation. The latter is hard to achieve, since the detector geometry is often not very well known. An experimental procedure was described by Egerton et al. [24] using a NiO standard. This procedure is basically very straightforward, but requires values for the ionization cross section and fluorescence yield, which are hard to find and typically exhibit severe uncertainties. To improve the accuracy of the solid angle measurement an in-depth study of these values is necessary.

In this work EDXS and the measured ζ -factors for six elements (Al, Si, Ti, Ga, As, Sr) were used to characterize the solid angle of the EDXS detectors of two TEMs, viz. the Super-X detector on the *Titan*³ and a Si(Li) detector on the *Tecnai F20*. The theoretical definition of the ζ -factor shows its indirect proportionality to the solid angle. To use this relation data for ionization cross sections, fluorescence yields and relative line intensity ratios are required, which is why an extensive research for literature and reliable databases was performed.

CHAPTER 2

Fundamentals of Energy-Dispersive X-ray Spectrometry in Transmission Electron Microscopy

Not only elastically or non-scattered electrons produce signals when being measured with a TEM; also inelastically scattered electrons generate information about the specimen and are used in analytical transmission electron microscopy (AEM). Analytical TEMs are usually equipped with an EDX spectrometer (using an Si, Ge or SDD detector) and/or an EELS system. X-rays and inelastically scattered electrons are detected to provide information about the elemental composition of a specimen. Furthermore, not only qualitative but also quantitative analyses are possible.

2.1 Generation of X-Rays

X-rays can be classified by their production either as characteristic X-rays or *bremstrahlung*. While characteristic X-rays are used for qualitative and quantitative analysis, *bremstrahlung* is generally an unwanted signal in X-ray spectrometry and has to be subtracted via background correction.

When a high-energy electron hits an atom, it may cause an inner shell ionization by creating a vacancy and leave the atom in an excited state. The atom will then return to its ground state by filling the vacancy with a higher shell electron and emitting a characteristic X-ray or an Auger electron. These processes are competing. The energy of characteristic X-rays is specific and corresponds to the energy difference of the participating shells. This property is used to identify elements by their radiative transitions. With regard to selection rules of electron transitions within an atom, X-rays of different energies are emitted. A complete list of possible electron transitions giving rise to K, L and M characteristic X-rays is shown in Figure 2.1.

The background in an X-ray spectrum comes from *bremstrahlung* arising of a change in momentum of the incident electrons, when they interact with nuclei in the specimen. During this process X-rays may be emitted. This radiation is continuous and can have any energy up to beam energy. One possibility to describe the likelihood of creating *bremstrahlung* is Kramers' law [41]:

$$N(E) = \frac{K \cdot Z \cdot (E_0 - E)}{E} \quad (2.1)$$

$N(E)$... amount of *bremsstrahlung* X-rays of a certain energy

K ... Kramers' constant: includes collection and processing efficiency
of the detector and absorption in the specimen

Z ... atomic number

E ... *bremsstrahlung* X-ray energy

E_0 ... electron beam energy

The intensity (number of photons) increases with decreasing energy but drops to zero at very low energies in a spectrum because low energy *bremsstrahlung* is absorbed in the specimen and the detector (see Figure 2.2) [73].

An EDX spectrum consists of a continuous background with superimposed characteristic X-ray peaks. The intensity of a characteristic X-ray line is given by the area under the corresponding peak less the background. One model to perform background subtraction is to define background windows in the spectrum (regions without characteristic X-ray peaks) and perform an analytical fit, which is then extrapolated to the whole spectrum using Kramers' law.

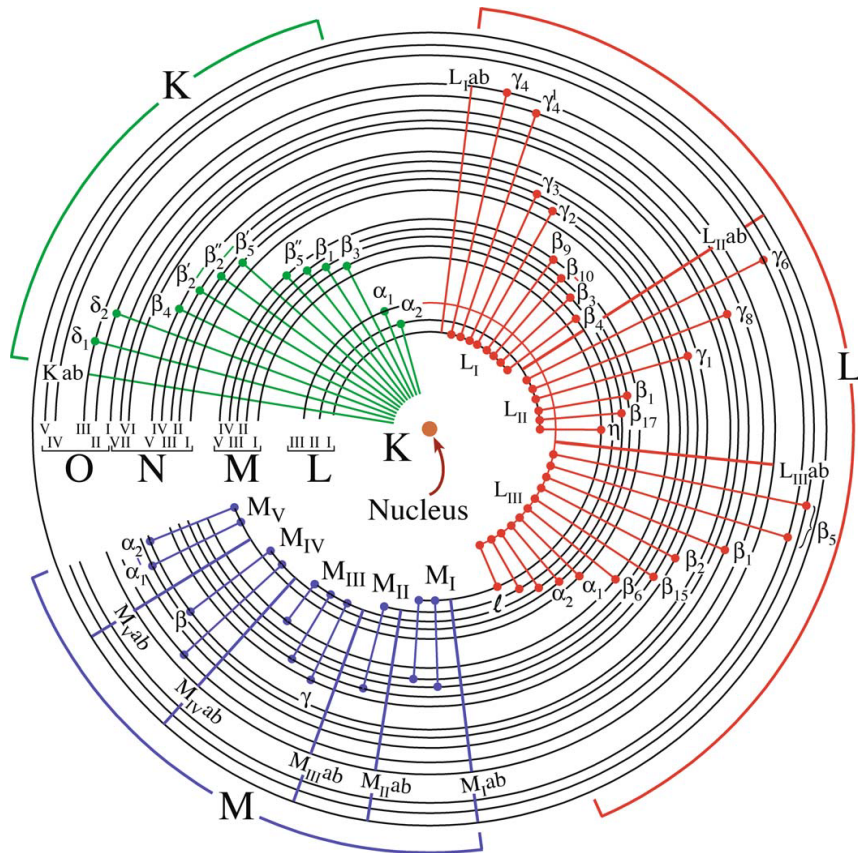


Figure 2.1: List of possible radiative transitions labeled with Siegbahn's nomenclature (see D. B. Williams et al. [73])

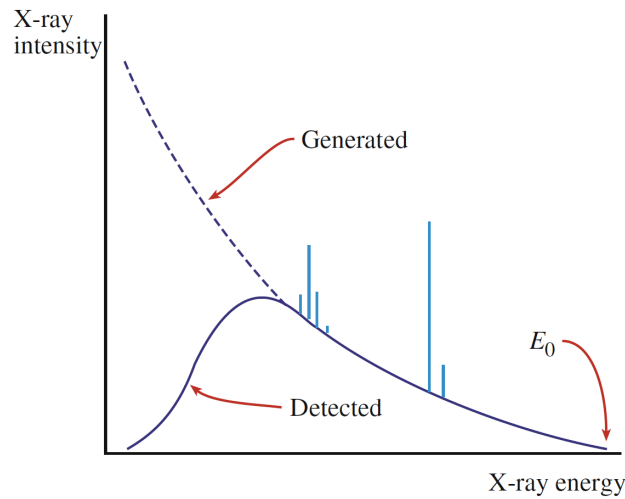


Figure 2.2: *Bremsstrahlung* intensity as a function of energy: Energies lower than approximately 2 keV are absorbed in the specimen and the detector and therefore cannot be detected; even though these X-rays are generated. E_0 is the beam energy. In addition superimposed characteristic lines at specific energies are shown (see D. B. Williams et al. [73]).

2.2 The Energy-Dispersive X-ray Spectrometer

An energy-dispersive X-ray spectrometer detects characteristic X-rays and *bremsstrahlung* and consists of three main parts, a semiconductor detector that is interfaced to signal-processing electronics and a computer. The computer acts as multichannel analyzer and stores and displays the spectra.

A schematic diagram of a conventional EDXS detector is depicted in Figure 2.3. The main component is the semiconductor detector crystal. An electron trap and a collimator assembly at the detector entrance protect the crystal against backscattered electrons and unwanted radiation. The detector can be designed either windowless or with a window, which separates the detector vacuum from the TEM column vacuum. When a X-ray hits the detector crystal a charge pulse proportional to the X-ray energy is generated. A field-effect transistor (FET) located behind the crystal converts the charge pulse into a voltage pulse and preamplifies it. The processing electronics separates the signal from other pulses, amplifies it, identifies it as a result from a specific X-ray energy and stores the digitized signal in the proper channel of the multichannel analyzer (i.e. computer). The result is a X-ray spectrum which is a histogram of X-ray counts versus energy.

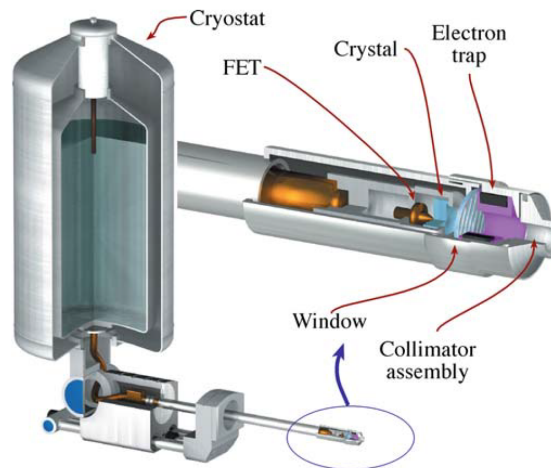


Figure 2.3: EDXS detector (see D. B. Williams et al. [73])

2.3 Semiconductor Detectors

Conventional TEM systems use silicon-lithium (Si(Li)), high-purity germanium detectors or the rather new silicon drift detector (SDD). Since Si(Li) and SDD detectors are used in this work, the following explanations are made only for those two.

When X-rays interact with the Si crystal, the predominant method of energy deposition is the transfer of electrons from the valence band to the conduction band, creating electron-hole pairs. Since Silicon is an indirect semiconductor, there are two relevant energy values concerning the creation of electron-hole pairs. The minimum band gap energy for the indi-

rect transition is 1.12 eV. Participating phonons are necessary for this process to provide the required momentum. More likely are direct transitions for the creation of an electron-hole pair with a required minimum band gap energy of 3.86 eV. [80] Since characteristic X-rays have energies above 1 keV, thousands of electron-hole pairs are generated by a single X-ray. Their quantity is directly proportional to the energy of the X-ray.

The Si(Li) detector is designed as a reverse-biased pin diode. The schematic diagram of a Si(Li) detector is shown in Figure 2.4(a). In the intrinsic region, which is between the p- and n-type region, the electron-hole pairs are generated. This region is called the active layer and is typically 3 mm thick. Si embodies acceptor impurities and therefore shows p-type behavior. Since impurities act as recombination traps for electron-hole pairs, Li is used as compensation to fill these sites. To separate the generated charges a voltage of 0.5 – 1 keV is applied between Au or Ni contacts, which are evaporated at the front and the back side of the crystal. During the fabrication process a p-type and n-type layer at the front and the rear side of the crystal are created, which do not contribute to the charge pulse of the incoming X-ray. These regions are also called dead layers. Si(Li) detectors need to be cooled (usually with liquid N₂). Without cooling thermal energy would trigger electron-hole pairs, which again would cause a noise level outshining the characteristic X-ray signal. Furthermore, the applied bias would cause Li atoms to diffuse at room temperature nullifying the intrinsic properties. Also the noise level in the FET would swamp low-energy X-ray signals [73].

The SDD consists of concentric rings, made of p-doped Si, located on the rear side of a n-Si single crystal (see Figure 2.4(b)). A bias voltage is applied at the front and the rear side, causing the device to get depleted from charge carriers. Another electric field generated by the concentric rings, which is parallel to the surface drives electrons generated by X-rays towards a small sized collecting anode in the middle of the detector [44].

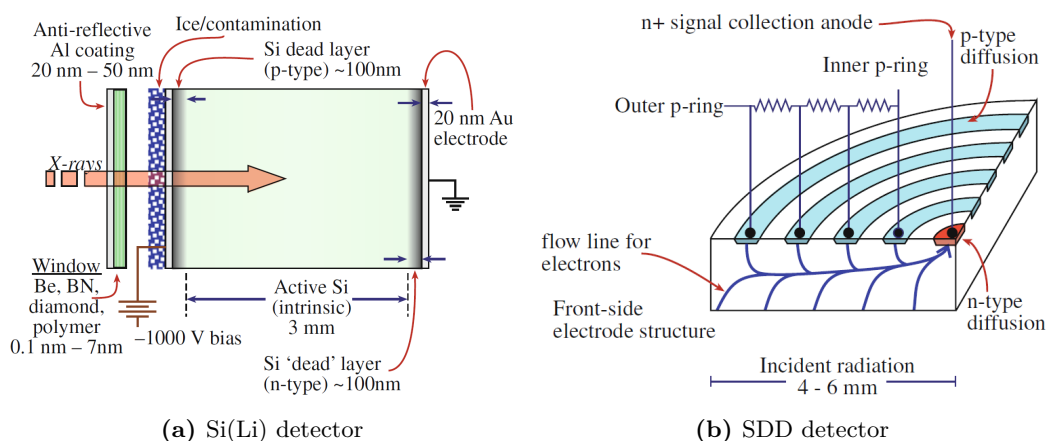


Figure 2.4: Schematic diagrams of two different EDXS detectors (see D. B. Williams et al. [73])

The anode has a much smaller capacitance than the large anode at the back side of a Si(Li) detector, because the device capacitance is directly related to its size. Since the electronic noise is proportional to the square of the capacitance, a better resolution and a faster detection are possible. The small noise signal enables operating temperatures that are readily achieved with a peltier device (e.g. -30°C).

2.4 Detector Efficiency

The detector efficiency describes the sensitivity of the EDXS detector to incoming X-rays. It depends on various detector parameters, geometrical factors and the incoming X-ray energy. It considers the absorption of X-rays in different layers that are situated before the active layer (window, contact layer, dead layer) as well as the pass through of high energy X-rays without being detected. The detector efficiency for one X-ray entering the EDXS detector is expressed as a product of transmittance and absorption factors for each detector component calculated via Lambert-Beer's law [27, 73]:

$$\begin{aligned} \varepsilon_A = & \exp\left(-\frac{\mu}{\rho}\right]_W^A \rho_W t_W) \cdot \left\{ T + (1 - T) \exp\left(-\frac{\mu}{\rho}\right]_{Grid}^A \rho_{Grid} t_{Grid}\right\} \\ & \cdot \exp\left(-\frac{\mu}{\rho}\right]_{Con}^A \rho_{Con} t_{Con}) \cdot \exp\left(-\frac{\mu}{\rho}\right]_{DL}^A \rho_{DL} t_{DL}) \\ & \cdot \left\{ 1 - \exp\left(-\frac{\mu}{\rho}\right]_{AL}^A \rho_{AL} t_{AL}\right\} \end{aligned} \quad (2.2)$$

ε_A ... detector efficiency for a characteristic X-ray energy from element A

$\left[\frac{\mu}{\rho}\right]^A$... mass absorption coefficient (MAC) of the X-rays of element A in

W ... window; $Grid$... windowgrid; Con ... Contact layer;

DL ... dead layer; AL ... active layer

ρ ... density

t ... thickness

T ... transmittance of the window due to the grid

(typically 77% for ultrathin polymer windows and 100% for beryllium windows)

The first four terms of equation 2.2 describe the transmission of X-rays through the window (including reduced transparency due to the grid of the window), the contact layer and the dead layer of the detector. The last term describes the absorption of X-rays in the active layer, which is a precondition for their detection.

The detector efficiencies of a Si(Li) and an SDD detector are shown in Figure 2.5 as a function of X-ray energy. The Si(Li) detector has a crystal thickness of 3 mm and is equipped with an ultrathin polymer window AP3.3 from Moxtek. Its detector efficiency

(blue line) is reduced due to absorption in the low energy regions and increases with higher energies. Several absorption edges occur on account of the materials used in the crystal, the contact layer and the window. For energies higher than approximately 10 keV the window grid becomes transparent, which increases the efficiency and explains the occurring bump. At still higher energies (<20 keV) the detector efficiency declines due to the fact, that high-energy X-rays are also able to pass through the detector without creating an electron-hole pair.

The SDD (red line in Figure 2.5) is windowless with a crystal thickness of 450 μm . Comparing to the Si(Li) detector, the detector efficiency of the SDD increases faster in low-energy regions and several absorption edges do not appear thanks to the lack of the window. Since absorption in the crystal depends on its thickness especially with increasing X-ray energy the efficiency of an SDD decreases earlier than the Si(Li) detector.

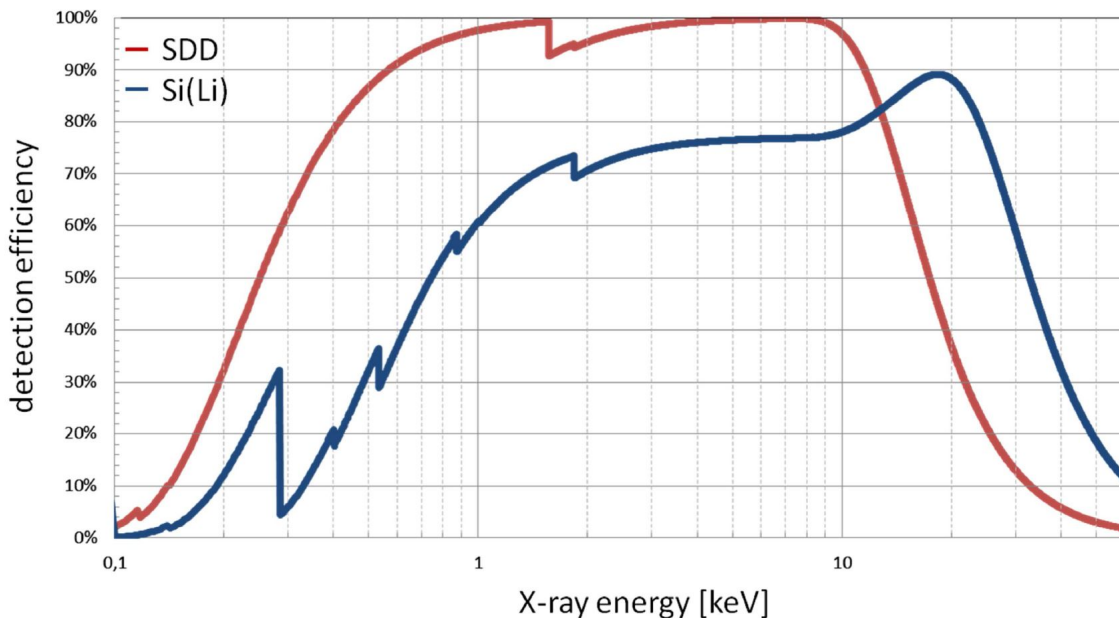


Figure 2.5: Detector efficiency of a Si(Li) and a SDD detector (see Fladischer [27])

2.5 The Solid Angle

The EDXS detector is placed close to the specimen in the microscope. In Figure 2.6 the interface between the EDXS detector and the TEM stage is displayed. When the electron beam hits the specimen, characteristic X-rays and *bremstrahlung* are emitted in all directions but only a small part of them is detected. The collection solid angle of the detector is the areal projection of the detector area (viewed from the point source in

the specimen) onto a bounding sphere that encloses the detector active area (see Figure 2.7)[78]. For this arrangement the solid angle is given as the following geometrical relation:

$$\Omega = \frac{S}{R^2} \approx \frac{A}{d^2} \quad (2.3)$$

S ... areal projection of the detector shape onto the bounding sphere

R ... radius of the bounding sphere

A ... active area of the detector (usually 30 mm^2)

d ... distance between the detector and the specimen

An approximation which substitutes S with the detector area A and R with the specimen-to-detector distance d is possible for large distances and small detector areas. However both assumptions are no longer valid for modern, large area detectors. For detectors close to the specimen the calculation of the solid angle of a detector is more difficult. It requires a profound knowledge of the detector geometry, which is often not very well known.

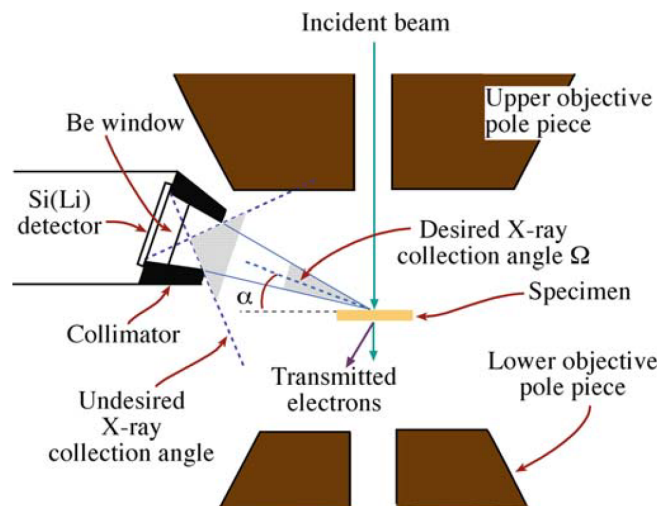


Figure 2.6: Schematic representation of the interface between the EDXS detector and the TEM stage (see D. B. Williams et al. [73])

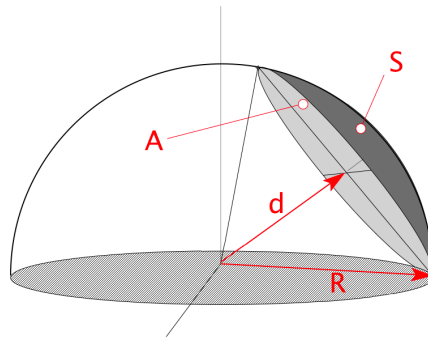


Figure 2.7: The solid angle is defined as the area S on a sphere of radius R , which is the projection of the detector area A at a distance d from the point source (see Zaluzec [78] with the permission of N. Zaluzec)

Zaluzec [76, 78] proposed analytical formulas to calculate solid angles for several detector geometries. Conway [20] analytically derived a line integral for the solid angle subtended by a surface detector of arbitrary shape.

The collectable fraction of generated X-ray signals is a major limitation regarding X-ray analysis in TEM. Several attempts were made to improve the collection efficiency in recent years. Three of them are schematically shown in Figure 2.8. Kotula et al. [40] proposed an annular SDD detector positioned above the specimen, whereas Zaluzec [77] placed his π Steradian detector after the specimen in the electron-optical beam line. Harrach et al. [32] integrated four SDD detectors in the conventional detector position around the specimen. This geometry is commercially sold by FEI. For further information, refer to Watanabe [69].

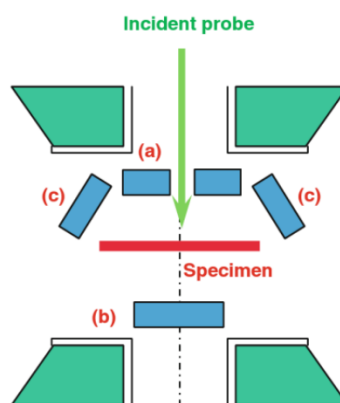


Figure 2.8: Recently proposed configurations of EDXS detectors: (a) annular detector above the specimen [40], (b) post-specimen detector [77], (c) multiple detectors at conventional positions (see Watanabe [69])

The actual solid angle including the impact of the real interface of the TEM-EDXS system can be measured. Egerton et al. [24] introduced a procedure using NiO as a test specimen for the characterization of EDXS detectors, including the measurement of the solid angle. For this determination the current of the incident electron beam has to be measured and the specimen thickness, the ionization cross section and fluorescence yield (see chapter 3), the density of the specimen as well as its quantitative composition has to be known. A measurement of the number of characteristic X-rays of one particular line series (in Egerton's case Ni-K lines only) leads to a determination of the solid angle via:

$$\Omega = \frac{I_K}{ntQ\omega D_e} \quad (2.4)$$

I_K ... X-ray intensity (Ni-K)

n ... amount of atoms of a certain element per volume unit (Ni atoms per cm³)

t ... thickness of the specimen

Q ... ionization cross section (for the Ni-K shell at the incident beam energy)

ω ... fluorescence yield

D_e ... total electron dose during acquisition

The total electron dose D_e is defined as:

$$D_e = N_e I_p \tau \quad (2.5)$$

N_e ... number of electrons in one unit of electric charge

I_p ... beam current

τ ... acquisition time

Egerton et al. [24] provide values for the ionization cross section and fluorescence yield of Ni-K. Since data for these parameters are hard to find and typically exhibit severe uncertainties, the reliability of these values is not evident.

Furthermore the collection efficiency depends on the position of the specimen relative to the detector. The rate of detected X-rays (and subsequently the magnitude of the solid angle) is decreased due to shadowing of the specimen holder, the tilting away from the detector and/or the use of a detector window with a grid.

2.6 Quantitative X-ray Analysis Using ζ -Factors

Once a qualitative analysis is performed and the peaks of an EDX spectrum are assigned to their corresponding elements, the quantitative analysis gives the opportunity to determine the concentration of the elements in the specimen. Typically, a first step is to remove the background originating from the *bremsstrahlung*. After that the peak intensities are

measured by integration over those peaks. Finally concentrations are calculated by a quantification method. The most popular quantification techniques are the Cliff-Lorimer [19] and the ζ -factor method [70]. The latter is used to determine the solid angle in this thesis.

Assuming that the thin-film criterion is valid in a specimen, meaning that absorption and fluorescence are negligible, the measured characteristic X-ray intensity is proportional to the mass-thickness and the composition. Therefore, the mass-thickness can be expressed as:

$$\rho t = \zeta_A \frac{I_A}{c_A D_e} \quad (2.6)$$

ρt ... mass thickness (ρ ... density, t ... thickness)

ζ_A ... proportionality factor

I_A ... intensity of the characteristic X-ray line of element A

c_A ... concentration of element A (mass fraction)

D_e ... total electron dose (see Equation 2.5)

Moreover the intensity of characteristic X-rays originating from element A can be theoretically described by [28]:

$$I_A = N \frac{Q_A \omega_A a_A}{A_A} c_A \rho t D_e \left(\frac{\Omega}{4\pi} \right) \varepsilon_A \quad (2.7)$$

N ... Avogadro's number

Q_A ... ionization cross section

ω_A ... fluorescence yield

a_A ... relative line intensity ratio

A_A ... atomic weight

$\Omega/(4\pi)$... collection efficiency: solid angle in the whole 4π space

ε_A ... detector efficiency

By comparing equations 2.6 and 2.7, the ζ -factor is expressed as:

$$\zeta_A = \frac{A_A}{N Q_A \omega_A a_A \left(\frac{\Omega}{4\pi} \right) \varepsilon_A} \quad (2.8)$$

The parameters in the ζ -factor are either related to X-ray generation or to X-ray detection. The ζ -factor depends on the electron beam energy (which affects the ionization cross section

Q_A) and the X-ray energy (which influences the detector efficiency ε_A), but is independent of the total electron dose, specimen composition, thickness and density. The parameters Q_A , ω_A and a_A and their determination are explained in detail in chapter 3.

Assuming a specimen with two compounds A and B (with concentrations $c_A + c_B = 1$) mass thickness and compositions are expressed as:

$$\rho t = \frac{\zeta_A I_A + \zeta_B I_B}{D_e}, \quad c_A = \frac{\zeta_A I_A}{\zeta_A I_A + \zeta_B I_B}, \quad c_B = \frac{\zeta_B I_B}{\zeta_A I_A + \zeta_B I_B} \quad (2.9)$$

This approach leads to a straightforward method for quantification and can be expanded to any multi-component specimen. Only X-ray intensities are necessary once the ζ -factors are known for the microscope. The mass-thickness is obtained simultaneously at the cost of knowing the electron dose and the specimen thickness in the analyzed region can be determined if the density is known.

If X-ray absorption within the specimen cannot be neglected an absorption correction must be performed. Watanabe et al. [70] give a detailed description of their iterative process concerning this matter. Since absorption correction was not necessary during this work it won't be further discussed.

2.7 How to Determine the Solid Angle via ζ -Factors

Equation 2.8 can be used to obtain the solid angle of an EDXS detector, if all other parameters are known, by remodelling it into the following form:

$$\Omega = \frac{4\pi \cdot A_A}{\zeta_A N Q_A \omega_A a_A \varepsilon_A} \quad (2.10)$$

This procedure has the advantage over Egerton's approach [24], that ζ -factors are constants per element for a certain EDXS system, whereas Egerton's measurements rely on single spectra from the NiO specimen using only the Ni-K line for solid angle determination. Using several ζ -factors for different elements increases the accuracy of this approach.

While values for Avogadro's number and atomic weight are simple to acquire, obtaining reliable data for ionization cross sections, fluorescence yields and relative line intensity ratios is more challenging (see chapter 3) and reliable values are crucial. The detector efficiency can be calculated via equation 2.2.

ζ -factors must be experimentally determined using equation 2.6. Therefore the used specimens have to be well known in density and composition. The X-ray intensity, total electron dose as well as the thickness has to be measured. After obtaining data for all appearing parameters the solid angle can be calculated separately for each element. Averaging over the values from all elements allows a precise and reliable determination of the solid angle.

CHAPTER 3

Databases

The determination of the solid angle via equation 2.10 requires data for: relative line intensity ratios, fluorescence yields and ionization cross sections. Egerton et al. [24] (see equation 2.4) used values for the fluorescence yield of Ni-K by Bambynek et al. [3]. To reduce uncertainties Egerton et al. [24] took averages from four different sources for the ionization cross sections. Watanabe et al. [70] even implemented 22 different models of ionization cross sections and fit the theoretically evaluated ζ -factors to the experimentally ones. It is obvious that obtaining trustworthy values, especially for ionization cross sections, is a crucial subject.

Therefore, reasonable values were obtained from searching databases and performing a literature research. Required were full sets of data concerning different energies and/or atomic numbers. The origin of data has to be given by publications and references as well as an estimation of their uncertainties. Within this section not only an overview of all found values shall be given but also a description of the finally chosen databases and programs as well as their theoretical background.

3.1 Relative Line Intensity Ratios

When atoms in a specimen are ionized in the K shell and return to their ground state through radiative transitions, they emit either K_α or K_β X-rays. The ratios of their intensities are not haphazard, but follow the probability ratios, in which these transitions occur. They are called *relative line intensity ratios*. These fractions can be calculated for all kind of transitions in different shells and subshells. The relation of K_α X-rays and the total intensity of the K spectrum is commonly used and given as

$$a = \frac{I(K_\alpha)}{I(K_{tot})}, \tag{3.1}$$

a . . . relative line intensity ratio
 $I(K_\alpha)$. . . intensity of K_α X-rays
 $I(K_{tot})$. . . total intensity of K X-rays

It is common practice in EDX quantification to use only intensities of the highest signal in a shell (e.g. K_α for the K shell). In order to do so relative line intensity ratios have to be known.

Relative X-ray intensity ratios can either be experimentally determined by measuring the ratio between particular X-ray intensities in a spectrum or calculated from the ratio between X-ray emission rates [79]. Comparing calculated and semiempirical data to experimental values, the available quantity of theoretical data predominates over experimental ones. A general recommendation for the usability of data of specific publications was not to be found during this literature research, but it shall be mentioned here that values from Scofield [61, 62, 64, 65] are used more often than others because of their completeness. Among this wide field of scientific publications about relative line intensity ratios, the compendium of Zschornack [79] may give an overview of the most relevant ones up to 2007. A few of them shall be mentioned here.

Schreiber et al. [60] developed equations for calculating intensity ratios for K, L and M shells from $Z = 11$ to 92. By using experimental and theoretical data, semiempirical equations are presented. Ratios are only given for total shells and can not be separated into fractions from different subshells.

Salem et al. [57] presented ratios calculated by least square fits to experimental data for K shells and L subshells up to $Z = 100$.

M shell X-ray emissions were calculated for six elements between $48 \leq Z \leq 93$ by Bhalla [6] using relativistic Hartree-Slater wavefunctions and for ten elements by Chen et al. [13] using relativistic Dirac-Fock wavefunctions.

Experimentally derived ratios for M spectra for rare earth elements are discussed in detail in Wendt [71]. For soft X-rays in energy region from 100 – 700 eV Aßmann et al. [2] reveal that measured line intensities of L and M lines differ up to two orders of magnitude from theoretical data.

Scofield [61, 62, 64, 65] made extensive calculations for radiative transitions using the consistent field model for K, L and higher shells.

A combination of values from Aßmann et al. [2], Scofield [61, 62, 64, 65], and Wendt [71], provided in the database of the software *MA-Table* [26], was used in this work. Ratios from Scofield [61, 62, 64, 65] are reliable for inner shells, but deviate significantly from experimental data for higher shells. These ratios were corrected or replaced by experimental values from Aßmann et al. [2] and Wendt [71]. The database provides intensity ratios referring to total intensities in each subshell. Scofield's theoretical models and a general outline of *MA-Table* are described in the following sections.

3.1.1 Theoretical Calculation via Hartree-Slater and Hartree-Fock

Looking at an atom with a vacancy in a certain inner subshell, this vacancy may be filled by an electron from a higher level accompanied by the ejection of an Auger electron or an X-ray. One way to calculate the rate of decay of vacancies accompanied by X-ray radiation is the Hartree-Slater theory [61]. Electrons are treated relativistically and the effect of retardation is included. Electrons are expected to move independently with their mutual interactions generated by a *central potential* (combining coulomb potential and screening of the nucleus by electrons). This occurring field can be determined by the *self consistent*

field method [1]: looking at two energy levels in an atom, a perturbation to the system (like excitation or ionization) results in a superposition of their wavefunctions, which can be expressed by a probability amplitude or a charge cloud. This charge cloud oscillates with a frequency equal to the energy difference between the two states, causing the emission of radiation. For finding the central potential an iterative procedure is used by making an initial guess about the form of the field and using it in the time-dependent Schrödinger equation to compute the wavefunctions of the levels; these results are then used to calculate the charge distribution and finally the potential. If initial guess and computed value differ from each other, the process is iterated until they match. The radial matrix elements of the transition operator between different subshells are then calculated by integrating the products of the initial and final wave functions and spherical Bessel functions [61]. The total radiative decay rate of a vacancy in a certain state is given by summing the radiative transition rates to this state of all the electrons from higher energy levels. The intensity ratio of K_α lines to their total K family is therefore calculated by the ratio of the sum of rates generated by the radiative transitions between K-L₂ and K-L₃ subshells and the total radiative K-vacancy decay rate.

All these calculations are based on the assumption that the electrons see the same potential in their initial and their final state and therefore some of the effects induced by the Fermi statistics are not taken into account. As an improvement, the restricted Hartree-Fock approach takes into account that their initial and final states differ from each other introducing a non vanishing overlap integral in their wave functions. This correction gives a more accurate estimation of matrix elements of the transition operator between different subshells [62, 63]. This influences the X-ray transition probabilities, since the rates of transition between two states are proportional to the overlap integrals. For further information about the Hartree-Fock and Hartree-Slater methods see [64, 65].

3.1.2 Available Data from *MA-Table*

Values for intensity ratios have been taken from the EDX spectra simulation program *MA-Table* [26] for scanning electron microscopes (SEM) written by and based on Eggert [25].

MA-Table is able to display X-ray line energy positions, allows element and line searches, shows overlaps of lines coming from different elements and provides values for shell excitation energies, mass absorption coefficients and relative line intensity ratios between lines of a series. It calculates excitation processes through electron impact and their influence to the relative heights of X-ray lines. By means of the built-in P/B fundamental parameter model for characteristic radiation and *bremsstrahlung* a complete spectrum simulation is possible, including stochastic processes of X-ray emissions and contributing artefacts of the EDX spectrometer.

When calculating minimum detection limits and the analysis depths, excitation conditions, specimen geometry overlap situations with other elements are taken into account. This simulated data acquisition depends on count rate and acquisition time. It is possible to switch between a simulation with stable electron beam-current or changing count-rates depending on acquisition conditions.

MA-Table provides a complete database for relative intensity ratios. Data comes from

Scofield [65] (a mixture of Hartree-Fock and Hartree-Slater calculations), but has been improved for L and M shells by measured values of Aßmann et al. [2] and Wendt [71] in cases where experimental and theoretical values were not coinciding. The software uses a notation for the ratios where summing up all the values within a subshell is equal to one or in other words the rates of single transition lines weighted against the total radiative vacancy decay rate. A partial view of the graphical user interface of *MA-Table* is given in Figure 3.1 showing EDXS data for X-ray line energies of Ga and their relative line intensities.

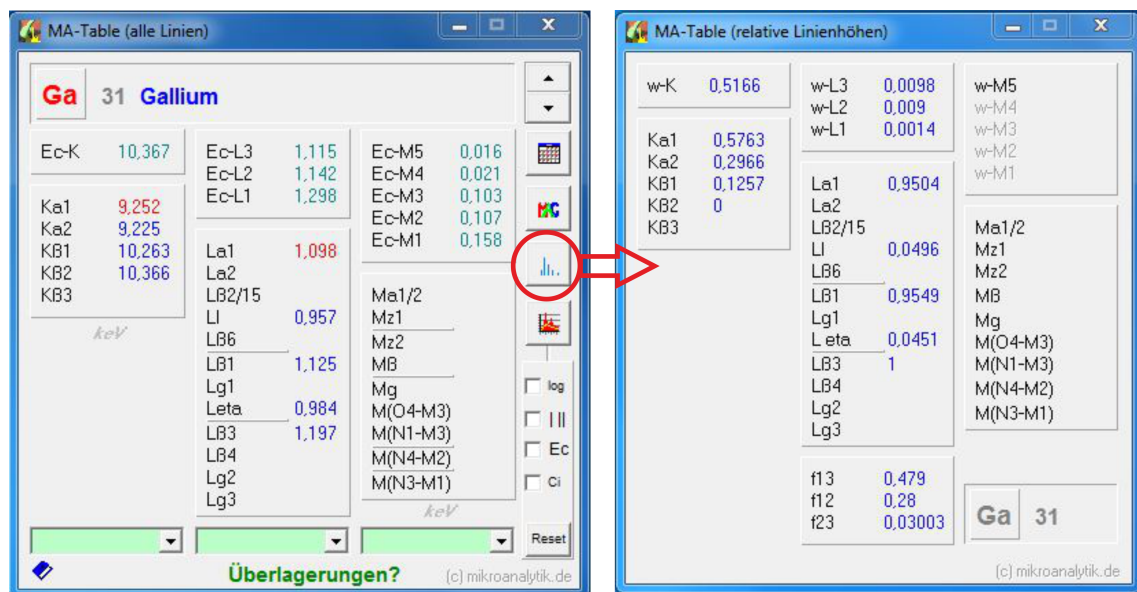


Figure 3.1: Two windows of *MA-Table* showing EDXS relevant data

Left image: Energies of Ga X-ray lines

Right image: Relative line intensity ratios for Ga

Validation of Data

Uncertainties concerning relative intensities are not given in the publication of Eggert [25]. Pia et al. [53] performed a quantitative validation of K and L shell radiative transition probability calculations according to the theoretical Hartree-Fock and Hartree-Slater methods against experimental data. They used χ^2 tests with a confidence level of 95 % to find out how often the null hypothesis (i.e. the calculations fit to experimental data) is rejected. They showed that for transitions directly compared to experimental data the null hypothesis is rejected in 53 % of the test cases for the Hartree-Slater calculations, but in only 6 % of the cases for Hartree-Fock.

In the publications by Scofield [61, 64, 65] radiative rates are accurate to approximately 2 – 10 % for K shells but become worse moving to outer shells. For low-Z elements and electrons in the outer shells the inaccuracies are highest.

Table 3.1 shows relevant values taken from the database which were used in the calculations of the solid angles acquired during this work.

Table 3.1: Relative intensity ratios for K_α lines of six elements taken from *MA-Table* and used for solid angle calculations. Inaccuracies of approximately 10 % can be assumed.

Element	$\frac{K_\alpha}{K}$
Al	1
Si	1
Ti	0.8806
Ga	0.8729
As	0.8651
Sr	0.8453

3.2 Fluorescence Yields

For an existing vacancy in a certain subshell radiative and nonradiative relaxation processes are possible. The probability of emitting a characteristic X-ray (i.e. undergoing radiative transitions) is called *fluorescence yield*. It increases with the atomic number Z , whereas the probability for a nonradiative transition (Auger electron) has an opposing trend. Their behavior is shown in Figure 3.2.

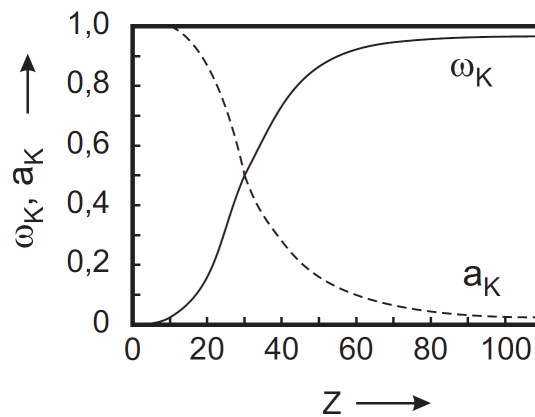


Figure 3.2: K-shell fluorescence yields ω_K and K-shell Auger yields a_K as a function of the atomic number Z (see Zschornack [79])

An overview of publications about fluorescence yields shall be given here. The first three

of the four here presented works are reliable compendia, which give a good overview of available values in their time. The fourth one (Livermore Evaluated Atomic Data Library (EADL)) is a state-of-the-art database used and recommended by the National Institute of Standard Technology (NIST). Similar to data for relative line intensity ratios a general recommendation for the use of certain data was not to be found.

Bambynek et al. [3] published an extensive compilation of data for fluorescence yields for K, L and M shells and radiationless and radiative transition probabilities, a state-of-the-art collection in 1972. A detailed explanation of theoretical calculation of average fluorescence yields with and without including Coster-Kronig transitions as well as calculations of transition probabilities are given. Experimental methods for measuring fluorescence yields, their evaluation and tables of experimental data collected from different sources and semi-empirical fits are presented.

Krause [42] presented a consistent set of values of atomic radiative and nonradiative yields for K shells (from $Z = 5 - 110$) and L subshells (from $Z = 12 - 110$) compiled from a broad compilation of experimental and theoretical data. Source material until 1977 was considered. Additionally he provided a reference list of relevant published papers between 1972 and 1977.

Hubbell et al. [36] compiled a comprehensive list of sources for fluorescence yield data published from 1978 to 1993. Comparisons between measurements, fits to experimental data and theoretical models for average fluorescence yields for the K, L, and M shells (not subshells) are presented. In addition their own fitting model is presented, in which selected measured values are fitted by least squares to polynomials as a function of the atomic number.

The EADL [52] is a subdatabase of the Evaluated Nuclear Data Library (ENDL) family [34], which includes an entirely consistent database for photon and electron interaction plus atomic relaxation. The EADL provides calculated subshell and relaxation data for isolated neutral atoms for elements $Z = 1 - 100$. Fluorescence yields are given for every subshell of K, L, M and higher shells.

Given the fact that the EADL contains fluorescence yields for every subshell from a consistent set of data and thanks to the recommendation of the NIST [56] we decided to use these values for our solid angle calculations.

3.2.1 Calculating Fluorescence Yields from Transition Probabilities and Widths

A vacancy in an atomic subshell leads to a series of radiative and non radiative transitions when the vacancy moves to outer subshells and the atom relaxes to a stable state. Radiative transitions manifest themselves by photon emissions whereas nonradiative transitions release an additional electron resulting in two electron vacancies in the atom. If the initial and the second vacancy are in different shells, this is called Auger process; if they are in the same shell, it is a Coster-Kronig transition. Relaxation data may be calculated from partial transition rates S (see chapter 3.1.1), which can be converted into partial widths Γ through the uncertainty principle $\Gamma = \hbar S$ [79].

Let $\Gamma_r(i,j)$ be the partial width of a radiative transition where a vacancy in subshell i moves to subshell j resulting in an emission of an X-ray and $\Gamma_{nr}(i;j,k)$ be the partial width of a nonradiative transition, with a vacancy in subshell i moving to subshell j causing an

emission of an electron from subshell k . The radiative and nonradiative widths for subshell i are then calculated by

$$\Gamma_r(i) = \sum \Gamma_r(i,j), \quad (3.2)$$

$$\Gamma_{nr}(i) = \sum \Gamma_{nr}(i,j,k) \quad (3.3)$$

and the total width is

$$\Gamma_t(i) = \Gamma_r(i) + \Gamma_{nr}(i) \quad (3.4)$$

Three different fluorescence yields are defined for a subshell [52]:

1. *Direct yield*: it includes all emitted photons coming from transitions filling a certain vacancy. The direct yield is defined as

$$\omega_i = \frac{\Gamma_r(i)}{\Gamma_t(i)} \quad (3.5)$$

2. *Enhanced yield*: it includes photons caused by transitions filling either the initial vacancy or any other vacancy within the same shell that has been created as a result of the initial vacancy. They result from radiative or Coster-Kronig transitions between subshells of the same shell. The binding energies of subshells in the same shell are very similar. Therefore it is experimentally difficult to differentiate between direct and enhanced yields.
3. *Total yield*: it includes not only all photons emitted caused by transitions filling the initial subshell vacancy but also any other vacancy within any subshell that has been created by the initial vacancy. The total yield may include additional photons but they are of lower energy and can be separated from the direct and enhanced yields in experimental observations.

3.2.2 The Database EADL

The EADL [52] provides data for isolated, neutral atoms of elements from $Z = 1 - 100$. It contains subshell and relaxation parameters as well as energy deposition terms. It contains basic subshell parameters like electron number, binding energy, kinetic energy, and expectation value of the radius. Furthermore it includes transition probabilities as well as the level widths for radiative and nonradiative transitions, fluorescence yields (derived from the transition probabilities) and energy deposition terms (derived from both transition probabilities and binding energies). Radiative transition rates were taken from Scofield [61, 64, 65] and nonradiative transition rates from Chen et al. [14–18]. Since these rates overpredict the strength of Coster-Kronig transitions, fluorescence yields were modified via formulas given by Hubbell [35]. Figure 3.3 shows a graph for K shell fluorescence yields given in the EADL.

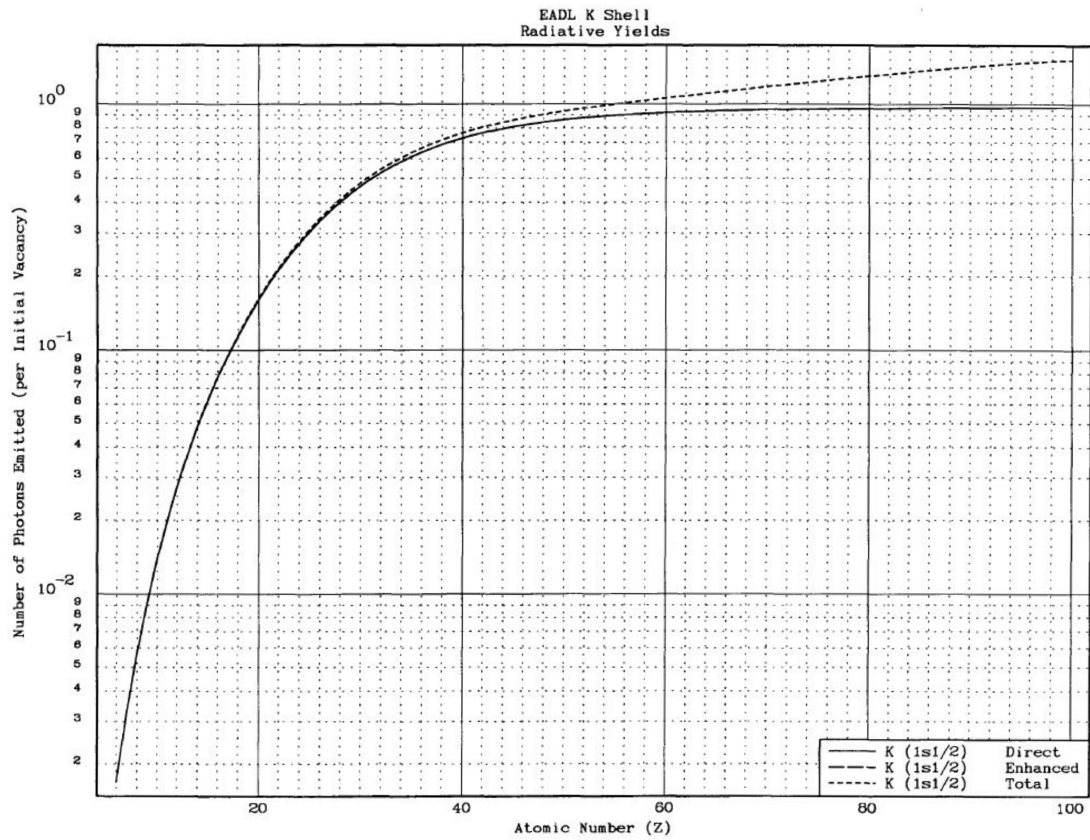


Figure 3.3: Perkins et al. [52] provides tables and graphs from the EADL. This graph shows direct, enhanced and total fluorescence yields for K shells of elements from $Z = 1 - 100$.

Uncertainties

According to Perkins et al. [52] the calculations of Chen et al. [14–18] for the nonradiative widths are known to better than 15 % if the inner shells do not decay by Coster-Kronig transitions; in that case the widths can be too large by a factor of two. These uncertainties directly affect the competition between radiative and nonradiative yields. Radiative rates from Scofield [61, 64, 65] are accurate to approximately 10 % for the K and L shell. For outer subshells inaccuracies up to 30 % are possible.

The values of direct fluorescence yields used for solid angle calculations in chapter 4.6 are displayed in Table 3.2.

Table 3.2: Direct fluorescence yields ω_K for the K shell of six elements taken from the EADL and used for solid angle calculations. Inaccuracies of approximately 10 % for the K shell are assumed.

Element	ω_K
Al	0.03715
Si	0.0485
Ti	0.2153
Ga	0.49729
As	0.55737
Sr	0.6857

3.3 Ionization Cross Sections

Characteristic X-rays from materials exposed to electron beams occur after the ionization of inner shells. Therefore the probability of ionization in particular shells or subshells, which is represented by the ionization cross section, is a relevant parameter. Ionization cross sections of a shell or subshell decrease with increasing atomic number and depend on the impact energy.

Although the ionization by electron impact was first investigated experimentally at the beginning of the twentieth century by Lenard [46] and Bloch [7] and theoretically by Thomson [68] in 1912, it took several decades until Dolder et al. [22] experimentally determined the first reliable electron impact ionization cross-sections for He^{1+} in 1961. The first quantum mechanical calculations of ionization cross-sections were made by Bethe [5] in 1930 and were modified by a relativistic correction by E. J. Williams [74] in 1933. Nowadays, a common practice for generating data for these cross sections is to perform computations via Monte Carlo codes. Available experimental information is quite restricted and uncertainties in experimental data are rather large. Liu et al. [48] compiled a list of experimental data for K-shell ionizations up to the year 1999, but values are limited to a few electron energies and relative differences in measurements from varying publications are often greater than their evaluated uncertainties. Experimental data for L- and M-shell ionizations are even scarcer. Several empirical and semi-empirical formulas have been released (e.g. [12, 30, 31, 33, 51]). Since they are based on measurements, they are only valid in particular energy ranges (where experimental information is available) and are influenced by the same uncertainties as the experimental data.

Powell [54, 55] provides a list and a review of nonrelativistic calculations for K- and L-shell ionization cross sections, whereas Scofield [66] describes a relativistic formulation for K- and L-shell cross sections of selected elements. Approximations based on the theoretical calculations have also been proposed by a number of authors (e.g. [37–39, 58]).

In 2014 the NIST released the database *NIST 164* [50] based on theoretical calculations [8, 9] with plane-wave Born approximations and distorted-wave Born approximations. The software provides data for ionization cross section for electron energies up to 1 GeV. A comprehensive uncertainty analysis was performed [49] giving figures of merit for the data used in *NIST 164*.

Since values for ionization cross sections from different publications diverge significantly especially for higher atomic numbers, their uncertainty analyses and validations are a relevant factor for a reliable choice of data. Llovet et al. [49] made an extensive and convincing uncertainty analysis concerning the values used in the database *NIST 164*. Therefore *NIST 164* was used for calculations of the solid angle and is described in the following sections.

3.3.1 Plane-Wave Born Approximation and Distorted-Wave Born Approximation

In 2008 Bote et al. [8] presented a method describing the computation of total inner shell ionization cross sections of atoms and positive ions by the impact of electrons and positrons with variable energies. In addition analytical formulas based on this method were published in 2009 [9].

In the theoretical models the target atom is described via the independent electron approximation which assumes that electrons of the target atom move in a central potential $V(r)$ described by a Latter tail corrected Dirac–Fock–Slater potential and yielding one-electron energy eigenvalues that are close to the experimental ionization energies. Using the same potential for initial and final atomic states provides orthogonality of one-electron wave functions which allows simplifications in the calculation of transition matrix elements, as well as a consistent description of exchange effects in the case of electron collisions. Ionization cross sections are calculated via the relativistic plane-wave Born approximation (PWBA) and the distorted-wave Born approximation (DWBA), where initial and final states of the target atom are represented as single Slater determinants. The PWBA describes the initial and final wave functions of the projectile as plane waves and the interaction H' between the projectile and the target atom as a first-order perturbation. In the DWBA, the difference $H'' = H' - V(r)$ is introduced as a perturbation and the projectile wave functions are described as distorted plane waves of the potential $V(r)$ [8, 9]. Calculations of inner shell ionization cross sections are done by using differential cross sections (DCS), which are expressed in terms of the generalized oscillator strength (GOS) and the transverse generalized oscillator strength (TGOS) depending on energy transfer W and the magnitude of the momentum transfer q . Numerical integration of the DCS over the allowed ranges of q and W finally yields ionization cross sections.

DWBA is only feasible for an overvoltage ratio lower than $U < 10$ [8], because of slower convergence of the partial-wave series and numerical instabilities at higher projectile energies. Noting that the atomic potential $V(r)$ distorts only partial waves with relatively small orbital angular momentum Bote et al. [8] formulated a composite algorithm to compute DWBA ionization cross sections by adding a correction term to the PWBA cross section due to this distorting effect. Electron collisions exchange effects are also accounted in the correction. This algorithm allows the numerical calculation of DWBA ionization cross sections for projectiles with kinetic energies in theory up to about $U = 25$. In practice calculation times get very high for $U > 16$ and calculations with DWBA are not reasonable. Values for projectile energies close to the ionization threshold ($U \approx 1$) are very difficult to calculate. If $U > 16$ the difference between DWBA and PWBA cross sections is mainly a result of the distortion of the projectile wavefunction by the atomic potential. Considering that the projectile gains (electron) or loses (positron) a certain kinetic energy when it

enters the potential, this effect may be partially taken into account by multiplying the PWBA cross section by an empirical energy-dependent scaling factor. It tends to unity in the energy range where the PWBA is expected to be reliable.

In a TEM overvoltage ratios of approximately 100 – 200 are common values.

3.3.2 *NIST 164* Database

Based on Bote et al. [8, 9] the database *NIST 164* [50] was released containing tables of inner shell ionization cross sections (K-, L- and M-subshells) of neutral atoms from $Z = 1$ to 99 by electron and positron impact. The range of kinetic energies extends from the binding energy up to 1 GeV.

A graphical user interface visualizes the contents of the database files. The GUI allows the user to select a certain source of binding energies (Dirac-Hartree-Fock-Slater [10, 67], Carlson [11] or [75]) or to define alternative binding energies for each shell. It is recommended to use binding energies from the Carlson compilation for atoms and molecules (e.g. in a gas) and data from Williams for solids [50]. Despite inner shell ionization cross sections which were relevant for this work, the database also provides cross sections for vacancy production in each subshell, for the emission of Auger electrons and for characteristic X-rays produced by a single vacancy. They are calculated from the ionization cross sections in the database and additional transition probabilities from Perkins et al. [52], X-rays energies from Deslattes et al. [21] (K- and L-subshells), Bearden [4] or Perkins et al. [52] (M-subshells) and Auger electron energies from Perkins et al. [52]. The values shown in Table 3.4 are taken from the database and were used for the calculations of the acquired solid angles during this work. An image of the GUI is shown in figure 3.4.

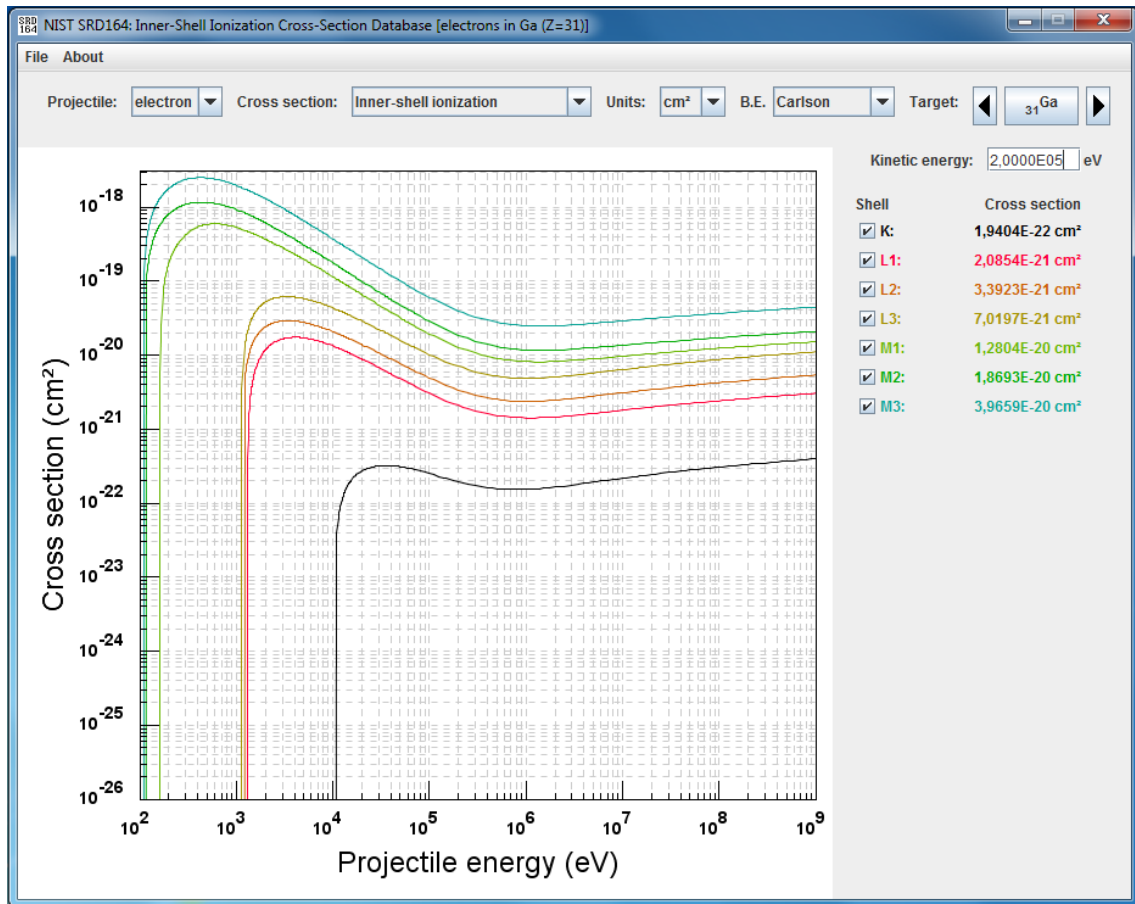


Figure 3.4: Graphical user interface of the database *NIST 164*. Species of projectile and cross section as well as possible data for binding energies and the required element can be chosen via the boxes in the upper bar. Putting in a value for the projectile's kinetic energy, shows directly the correspondent cross section values. A graphical demonstration of the run of different subshell cross sections is shown on the left side of the GUI. An export of the calculated values is possible.

Uncertainties for Ionization Cross Sections

Llovet et al. [49] made an extensive quantitative and graphical comparison of experimental K-shell, L-subshell, and M-subshell ionization cross sections with the corresponding values calculated from Bote et al. [8, 9]. They chose elements for which there were at least three (K-shells) or two (L- and M-subshells) mutually consistent sets of data available and determined root-mean-square (RMS) percentage deviations and mean percentage deviations between measured and calculated cross sections for each element. Eventually, they elaborated plots to show whether there are any systematic trends in percentage deviations as a function of overvoltage ratio or as a function of atomic number Z . For the K-shell 26 elements, for L-subshells eight elements and for M-subshells only three elements met the evaluation criteria. Neither their percentage deviations varied significantly with

overvoltage ratios nor the average of the RMS percentage deviations notably changed with atomic number. Results for average RMS deviations between the measured and calculated cross sections are listed in Table 3.3. For a reliable use of the database, they basically recommend that the overvoltage ratio should be greater than 1.02. Additionally the projectile energy should also be at least 50 eV larger than the ionization energy in order to avoid effects due to post-collision interactions in free atoms or molecules and screening effects in solids. For the sake of completeness it should be mentioned here, that Llovet et al. [49] also provide uncertainties for cross sections of X-ray production, vacancy production and emission of Auger electrons.

Table 3.3: Average RMS deviations between the measured and calculated cross sections [49]

	K-shell	L-subshells	M-subshells
Average RMS deviation [%]	10.3	15.0	23.5

The values shown in Table 3.4 are taken from the database and were used for the calculations of the acquired solid angles during this work.

Table 3.4: K-shell ionization cross sections Q of six elements for electron beam energies of 200 keV and 300 keV taken from *NIST 164* and used for solid angle calculations.

Element	Q at 300 keV [m ²]	Q at 200 keV [m ²]
Al	$1.82006 \cdot 10^{-25}$	
Si	$1.48697 \cdot 10^{-25}$	
Ti	$4.36998 \cdot 10^{-26}$	$5.04564 \cdot 10^{-26}$
Ga	$1.7186 \cdot 10^{-26}$	$1.94036 \cdot 10^{-26}$
As	$1.44074 \cdot 10^{-26}$	$1.61846 \cdot 10^{-26}$
Sr	$9.61025 \cdot 10^{-27}$	$1.05967 \cdot 10^{-26}$

3.4 Comparing Values Used by Egerton et al. [24] to the New Databases

As already mentioned in the beginning of this chapter Egerton et al. [24] used a the Ni-K line to experimentally determine the solid angle. Table 3.5 gives an overview of values for the ionization cross section at an electron beam energy of 200 keV and the fluorescence yield for the Ni-K shell used by Egerton and compares them to the values given by the databases *NIST 164* (ionization cross section) and *EADL* (fluorescence yield). They differ slightly, but not significantly from each other.

Table 3.5: A comparison of the values for the ionization cross section (at 200 keV) and fluorescence yield for the Ni-K shell taken from Egerton et al. [24] and the databases *NIST 164* and *EADL*.

	Egerton et al. [24]	<i>NIST 164</i> and <i>EADL</i>
Ionization cross section [m ²]	$2.55 \cdot 10^{-26}$	$2.59 \cdot 10^{-26}$
Fluorescence yield	0.414	0.40135

CHAPTER 4

Experiments

ζ -factors were measured for four different elements. The solid angles were calculated via these measured ζ -factors and the theoretical parameters (see chapter 3). Additionally, previously measured ζ -factors for Al-K ($Z = 13$) and Si-K ($Z = 14$) [43] were used to calculate the solid angles of the four quadrants of the Super-X detector.

4.1 Specimens

4.1.1 Choice of Samples

The determination of the solid angle via ζ -factor requires well characterized specimens. They need to be known in terms of composition and density, thinned to electron transparency, stable under the electron beam and should not oxidize, while being exposed to air. Furthermore, they should not contain elements used in microscope components. The X-ray-lines should not overlap and their energies should be within 2 to 15 keV to minimize possible absorption. In order to avoid channelling effects the specimens should be polycrystalline. In this work two materials were chosen. Their densities and compositions are listed in Table 4.1.

Table 4.1: Materials used for ζ -factor measurements

c ... concentration in percentage by mass [wt%]

ρ ... density [g/cm³]

Gallium Arsenide	GaAs $c_{Ga} = 48.20$ wt%, $c_{As} = 51.80$ wt% $\rho = 5.31$ g/cm ³
Strontium Titanate (STO)	SrTiO ₃ $c_{Ti} = 26.09$ wt%, $c_{Sr} = 47.75$ wt% $c_O = 26.16$ wt% $\rho = 5.12$ g/cm ³

The X-ray peaks for the K_α lines of GaAs, which are both usable for ζ -factor measurements, are at 9.25 keV for gallium and at 10.54 keV for arsenic. Since the O-K line suffers from absorption in STO, only the lines of Sr and Ti are used (Sr- K_α at 14.71 keV and Ti- K_α at 4.51 keV). Both materials are single crystals, hence they were tilted away from a zone axis in order to avoid channelling effects.

4.1.2 Specimen Preparation

The specimens were prepared from bulk material by means of a focused ion beam (FIB) using the *in situ* lift-out specimen preparation technique [29]. Two different shapes of the same material, a lamella and a needle, were needed to experimentally determine the ζ -factor.

To prepare a lamella a standard procedure was applied [29]. The preparation of a needle was executed likewise, but a circle pattern instead of a rectangle was used on the interface in order to obtain the shape of a cone. A typical overview image taken in the FIB after preparation is shown in Figure 4.1. The needles were bound either to a picoprobe pin-shaped tungsten specimen tip (GaAs) or on an omniprobe grid (STO). The omniprobe grids were assembled on the Hi-VIS holder (see the proximate chapter 4.2) for the *Titan*³ or the analytical double-tilt holder for the *Tecnai F20*. The picoprobe pin-shaped tungsten specimen tip was mounted onto the tomography specimen holder.

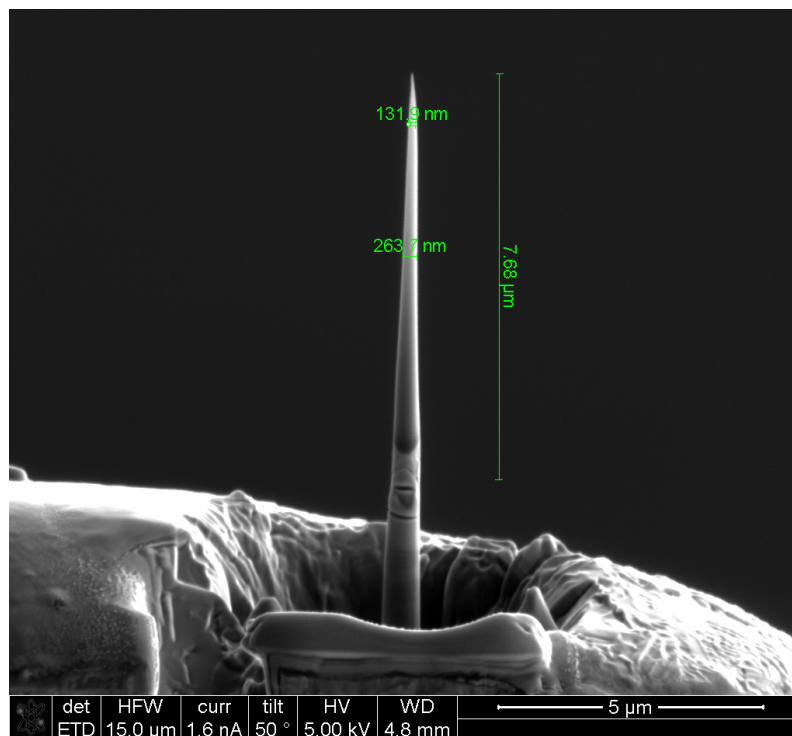


Figure 4.1: Needle after FIB preparation; still fixed on the bulk material. In the following preparation step it is released from the bulk and mounted on a grid or a specimen tip.

4.2 Used TEM-EDXS Systems

The following two systems were used for this work:

FEI Tecnai F20 (S)TEM

The *Tecnai F20* uses a Schottky field-emission gun (FEG) with a monochromator and operates at a voltage of 200 kV. It is equipped with a DigiScan II STEM controller, high angle annular dark field (HAADF), annular dark field (ADF) and bright field (BF) detectors and a high resolution Gatan Imaging Filter (GIF), which is an electron spectrometer for EELS and energy filtered transmission electron microscope (EFTEM).

Furthermore, the microscope houses a conventional EDXS detector from EDAX, which consists of a Sapphire Si(Li) detector. The active area of the detector is 30 mm² and the active layer is 3 mm thick. An ultrathin polymer window (AP3.3 window from Moxtek) is used.

FEI Titan³ (S)TEM

The *Titan³* is equipped with a high brightness Schottky X-FEG with a monochromator. Operating voltages are 60 kV, 80 kV, 200 kV or a maximum of 300 kV. It contains a Cs-probe corrector for high resolution STEM imaging, a DigiScan II STEM controller, several HAADF, ADF and BF detectors and a high resolution GIF Quantum electron spectrometer for EELS and EFTEM mapping.

The *Titan³* is equipped with a special EDXS detector system called Super-X detector, which consists of four windowless SDD detectors placed symmetrically around the optical axis (see Figure 4.2). Each quadrant has an active area of 30 mm² and a thickness of 450 μm.

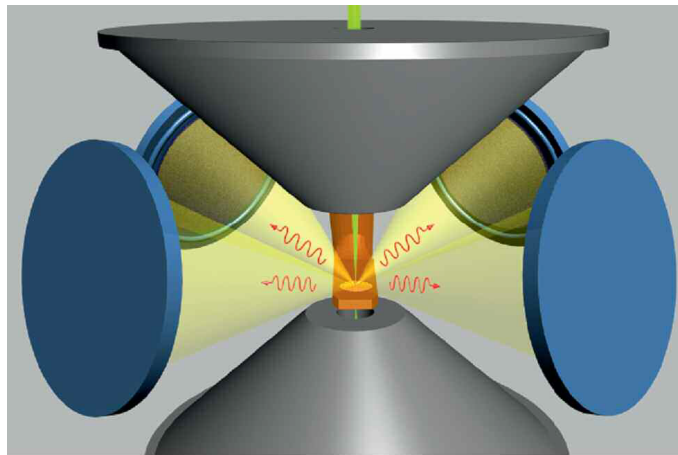


Figure 4.2: Schematic of the Super-X geometry: Four SDD detectors are arranged symmetrically around the sample (see Schlossmacher et al. [59])

Due to the holder shadowing effects reduce the amount of X-rays detected by the detector. In order to avoid these negative shadowing effects, the specimen is tilted towards the EDXS

detector during the measurements. Three different holders were used: (1) a standard analytical double-tilt holder for the *Tecnai F20*, (2) a tomography specimen holder, on which a picoprobe pin-shaped tungsten specimen tip was mounted (tilting is not necessary using this holder), (3) a Hi-VIS holder especially suited for the Super-X geometry at the *Titan*³. Since the four detectors are located symmetrically around the specimen, tilting to one side leads to greater shadowing on the opposite side when measuring with four detectors simultaneously. Therefore this holder shows cut out areas to increase the amount of detected X-rays in a zero tilt specimen position (see Figure 4.3).

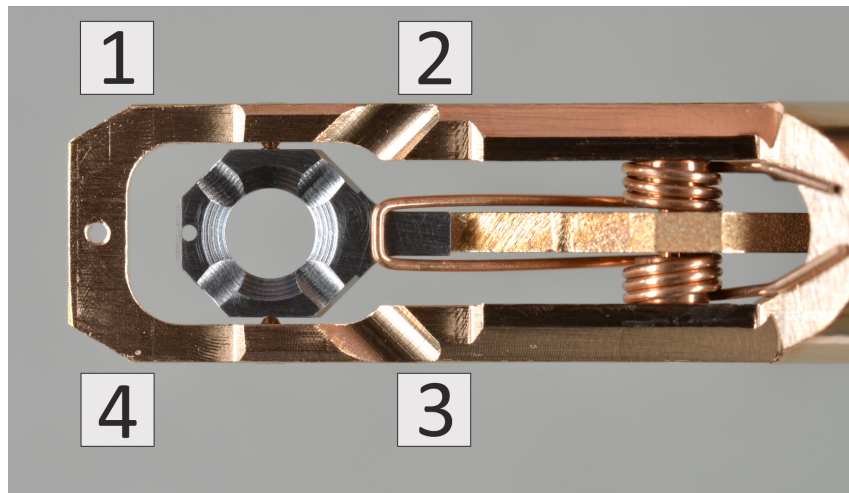


Figure 4.3: The new Super-X high visibility holder with cut out areas in direction to the indicated positions of the four Super-X detectors

4.3 Experimental Set-up

The measurements were performed in STEM mode on the FEI *Tecnai F20* and on the FEI *Titan*³. The parameters for the acquisition of EDXS and EELS data are listed in Table 4.2. When analyzing the lamellas and the needles of STO bonded on the omniprobe grid with the *Titan*³ the specimens were tilted to $\alpha = 15^\circ$ for spectrum acquisition with quadrant I and II and to $\alpha = -15^\circ$ for quadrant III and IV to avoid shadowing effects of the grid or the holder. While measuring with the *Tecnai F20* a tilt to $\alpha = 11^\circ$ for EDX measurements is required. Tilting is not necessary if the measurements are made using a needle mounted on the tomography specimen holder, which was the case for GaAs.

Table 4.2: Parameters used during measurements

	<i>Titan</i> ³	<i>Tecnai F20</i>
Specimen tilt angle α [°]	0 or ± 15	0 or ± 11
C1 aperture [μ m]	2000	2000
C2 aperture [μ m]	50	50
Camera length [mm]	29.5	50
Spectrometer entrance aperture [mm]	5	5
Dispersion EDXS [eV/channel]	5	5
Dispersion EELS [eV/channel]	0.25	0.2
Voltage [kV]	300	200

4.4 Acquisition of Required Data

To experimentally obtain ζ -factors the following parameters must be measured: the X-ray-line intensity of the K_α peak, the acquisition time, the beam current and the thickness of the sample.

EDX spectra were taken from the lamella. The current was measured with the drift tube of the GIF in the *Titan*³ and a calibrated CCD in the *Tecnai F20* respectively. The t/λ -method was used to obtain the thickness of the lamella. Since t/λ -maps contain only values for the relative thickness, the absolute thickness cannot be determined directly. Therefore the inelastic mean free path λ was acquired by using the a t/λ -map of a sample with a known thickness; in our case this was the cone shaped needle. The measured inelastic mean free path λ was then again used for the thickness evaluation of the lamella (see section 4.4.2). If absorption in the sample occurs during the acquisition of the X-ray spectrum, an absorption correction should be performed to receive the corrected X-ray intensities of the reduced peaks. The used correction method is only valid for planar samples. This was the reason why the X-ray spectrum was taken from the lamella and its thickness was evaluated by means of t/λ -maps and the needle. For the measurements with GaAs on the *Titan*³ a lamella and a λ value derived from the needle were used.

If an absorption correction is not necessary, the experiment can be performed only with the needle and measurements with the lamella, as well as t/λ measurements are no longer necessary. EDX spectra are acquired on the needle. The thickness can easily be measured by taking a profile of the HAADF image of the needle. Only the needle was used for measurements of GaAs on the *Tecnai F20* and of STO on both microscopes.

To avoid channelling effects electron diffraction patterns had to be evaluated to verify that the crystal orientation was far enough away from any zone axis. HAADF images of the needle with different tilt angles verified that it was rotationally symmetric. Therefore the GaAs needle on the picoprobe pin-shaped tungsten specimen tip was tilted to $\alpha = 0^\circ$ and $\pm 45^\circ$ and the STO needles on the omniprobe grid to $\alpha = 0^\circ$ and $\pm 25^\circ$ respectively.

4.4.1 Determining Peak Intensities of EDX Spectra

For the analysis of acquired EDX spectra the software Digital Micrograph (DM) was used. The background was calculated by Kramers' law (see equation 2.1 in chapter 2.1) and subtracted from the spectra. Intensities of the background corrected peaks are calculated via peak integration. Gaussian fits are made for the peaks using their peak maximum and their full width half maximum (FWHM). The intensities are calculated with:

$$I = \sqrt{2\pi} \cdot P_{max} \cdot \sigma \quad (4.1)$$

I ... intensity

P_{max} ... Maximum of the peak

σ ... Standard deviation of the peak, with $\sigma = \text{FWHM}/(2\sqrt{2\ln 2})$

FWHM ... full width half maximum

Figure 4.4 and Figure 4.5 show the calculated background as well as the determination of the Gaussian peaks. As represented in Figure 4.4 the peaks of As-K $_{\alpha}$ and Ga-K $_{\beta}$ are overlapping but it is possible to separate them from each other by a simultaneous fit. Taking into account the fits of the overlapping peaks did not change the calculated intensities. For the determination of the ζ -factors only the intensities of K $_{\alpha}$ peaks were used.

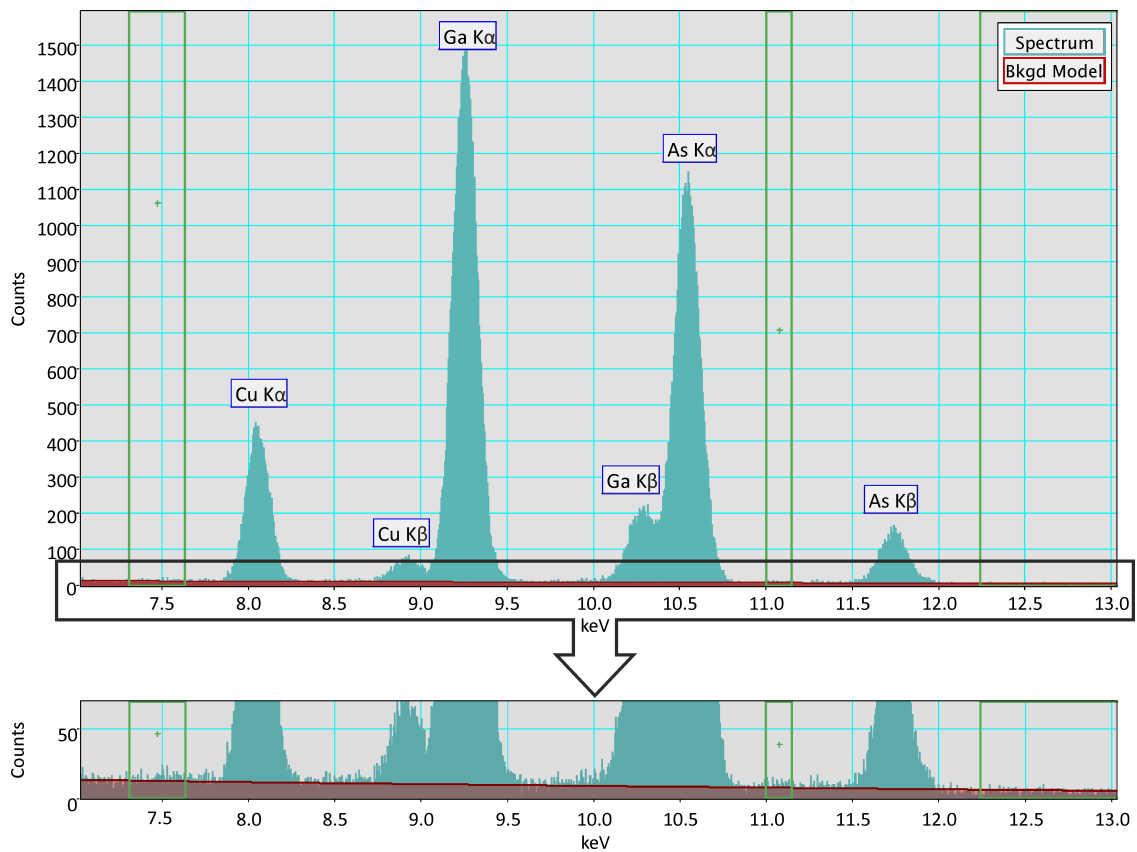


Figure 4.4: Background calculation via Kramers' law. Green rectangles indicate regions without peaks for the fit.

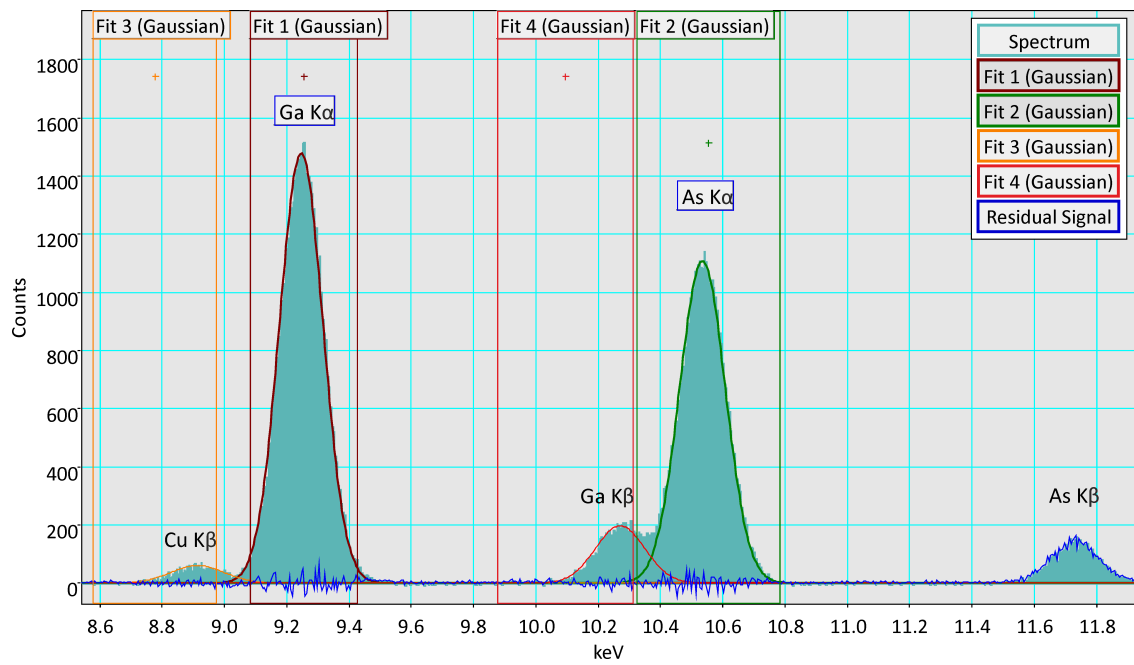


Figure 4.5: Gaussian fits to the relevant and to other overlapping peaks

4.4.2 Thickness Determination with t/λ Measurements

A direct absolute thickness determination is not possible when working with a lamella for measuring ζ -factors. One way to evaluate the relative thickness is acquiring t/λ measurements. Since the amount of transmitted inelastic scattered electrons depends on the thickness t and the inelastic mean free path λ of the specimen, it is possible to determine the relation

$$\frac{t}{\lambda} = \ln\left(\frac{\text{unfiltered}}{\text{zero-loss filtered}}\right) \quad (4.2)$$

by calculating the natural logarithm of the fraction of the unfiltered EELS spectrum (total intensity) and the zero-loss filtered EELS spectrum (intensity generated by elastic or non-scattered electrons)[23].

To get the absolute thickness of the lamella from a t/λ -map, the inelastic mean free path λ must be known. This value was determined by measuring t/λ -maps of the needle (see Figure 4.6). At first an EELS spectrum image was taken from a region of interest on the needle. From this spectrum image a t/λ -map was calculated with the software DM applying the reflected tail method for zero-loss filtering. Thanks to the cone shaped geometry of the needle its thickness is known in every point of the specimen. Therefore, the thickness was determined by taking a profile of the t/λ -map and measuring the width of the needle. The t/λ value, which is measured at the thickest point in the middle of the needle corresponds to this width. By knowing the thickness and the t/λ value at this point the inelastic mean free path λ was calculated. The absolute thickness of the lamella was determined by measuring t/λ -maps of the lamella and using the elaborated value for λ .

This procedure of thickness determination was not used for all specimens. For other specimens measurements were only done with the needle, where the thickness is known (see section 4.4).

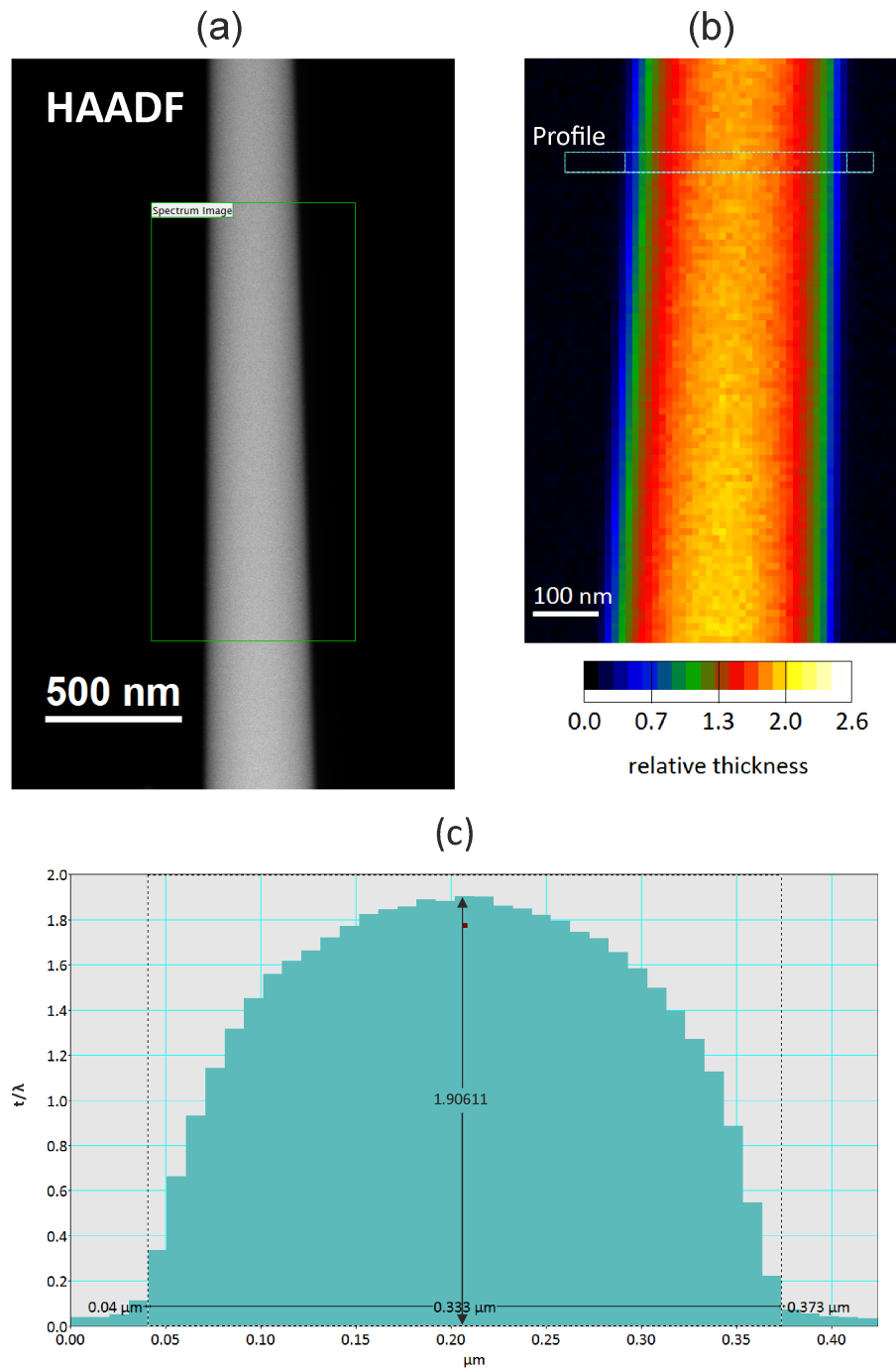


Figure 4.6: Process to calculate the inelastic mean free path λ from a needle shaped specimen: (a) The green rectangle in the HAADF image marks the area on the needle where an EELS spectrum image is taken. (b) From the relative thickness map (t/λ map) a profile is extracted. (c) The profile gives information about the thickness (width) of the needle and its maximum t/λ value in the middle of the needle. Thanks to the rotational symmetry of the rod, these two values correspond to each other and the in elastic mean free path λ can be calculated.

4.5 ζ -Factor Determination

ζ -factors were measured for the elements gallium, arsenic, strontium, and titan. When placing the specimens into the Hi-VIS holder (or the analytical double-tilt holder for the *Tecnai F20*) their orientation relative to the EDX system in the microscopes is a crucial factor with respect to shadowing effects. Hence, the microscopes were adjusted with respect to tilting and other parameters as described in section 4.3. EDX and EELS spectra as well as HAADF images were acquired. To ensure an adequate statistical distribution of counts EDX spectra with a live time between 190s and 740s were recorded. ζ -factors were determined using a lamella and a needle (including EELS spectra for thickness determination) when measuring with GaAs on the *Titan*³. All other measurements (GaAs on the *Tecnai F20* and STO on both microscopes) were done only with the needle (without EELS measurements). Both procedures are described in section 4.4. To determine the ζ -factors three different EDX spectra per Super-X quadrant were acquired. Two additional spectra for GaAs were taken with quadrant IV, where the current was varied between 118 and 220 pA. With the *Tecnai F20* four spectra were recorded.

An EDX spectrum of GaAs, measured with quadrant I of the Super-X detector of the *Titan*³ is shown in Figure 4.7. Various K and L lines of Ga and As as well as small Cu, Co and Fe peaks coming from components of the microscope are seen. The C peak is caused by contamination, whereas the O peak originates from oxidation of the specimen due to storing in air. In Figure 4.8 an EDX spectrum of STO is shown, which was also acquired with quadrant I of the Super-X detector. K and L lines of Sr, Ti and O and the already mentioned signals from the microscope appear. In addition an Al-K peak is visible, which originates from the detection of the specimen holder. The spectrum analysis and intensity calculation was done by subtracting the background via Kramers' law and by Gaussian fits as described in chapter 4.4.1. Only K_{α} lines of Ga, As, Sr and Ti were used for the intensity calculations. The O-K peak measured with STO could not be taken into account due to a necessary absorption correction. Based on equation 2.6, not only intensities but also composition, acquisition time, beam current, and mass-thickness need to be known for ζ -factor determination. Compositions were taken from stoichiometry and densities from Lide D. R. [47] (see Table 4.1). The beam current was measured with the calibrated CCD on the *Tecnai F20* and with the drift tube of the GIF on the *Titan*³. Measured values are listed in Table 4.3.

The resulting ζ -factors for K lines of Ga, As, Ti, and Sr are listed in Table 4.4. Although the four Super-X quadrants of the *Titan*³ should be located symmetrically to the specimen, their ζ -factors differ from each other; already small deviations in the distance to the specimen have an observable influence. Errors were determined using single standard deviation.

Table 4.3: Measured values from the samples GaAs and STO. I_p ... current τ ... acquisition time $I_{element}$... X-ray intensity (K_α)

t ... thickness of the specimen

GaAs						
	I_p [nA]	τ [s]	I_{Ga} [counts]	I_{As} [counts]	t [nm]	
Super-X Q1	0.178	198.0	51712	41494	92	
	0.176	197.6	62088	49511	121	
	0.176	198.6	50584	40350	100	
Super-X Q2	0.176	201.7	55471	44412	119	
	0.176	198.6	40262	31061	87	
	0.176	211.2	45648	32987	92	
Super-X Q3	0.175	194.3	52401	42361	111	
	0.175	192.2	51406	41125	112	
	0.174	202.9	55393	43972	120	
Super-X Q4	0.171	193.1	59021	46878	112	
	0.171	192.7	60408	48098	117	
	0.171	195.0	67857	54692	135	
	0.118	193.2	48342	38983	139	
Si(Li)	0.220	191.9	87078	70062	134	
	0.044	495.3	26705	24162	270	
	0.044	739.4	42858	39352	280	
	0.057	473.5	37521	33785	304	
	0.057	468.5	37339	34486	306	
SrTiO₃						
	I_p [nA]	τ [s]	I_{Ti} [counts]	I_{Sr} [counts]	t [nm]	
Super-X Q1	0.237	290.8	224317	104726	303	
	0.237	290.3	240801	111029	307	
	0.237	290.0	240602	111967	319	
Super-X Q2	0.236	291.0	230828	108668	328	
	0.236	291.3	223036	104917	317	
	0.236	291.6	210537	99477	304	
Super-X Q3	0.235	283.1	213605	106147	300	
	0.235	282.9	217777	106856	302	
	0.235	283.0	223792	110567	318	
Super-X Q4	0.234	281.5	252907	124862	315	
	0.234	282.6	236394	116074	294	
	0.234	282.1	240984	118407	300	
TF20	0.069	418.1	16158	12558	175	
	0.069	418.6	17563	13489	181	
	0.069	411.0	18025	13964	185	
	0.069	412.6	17237	13495	172	

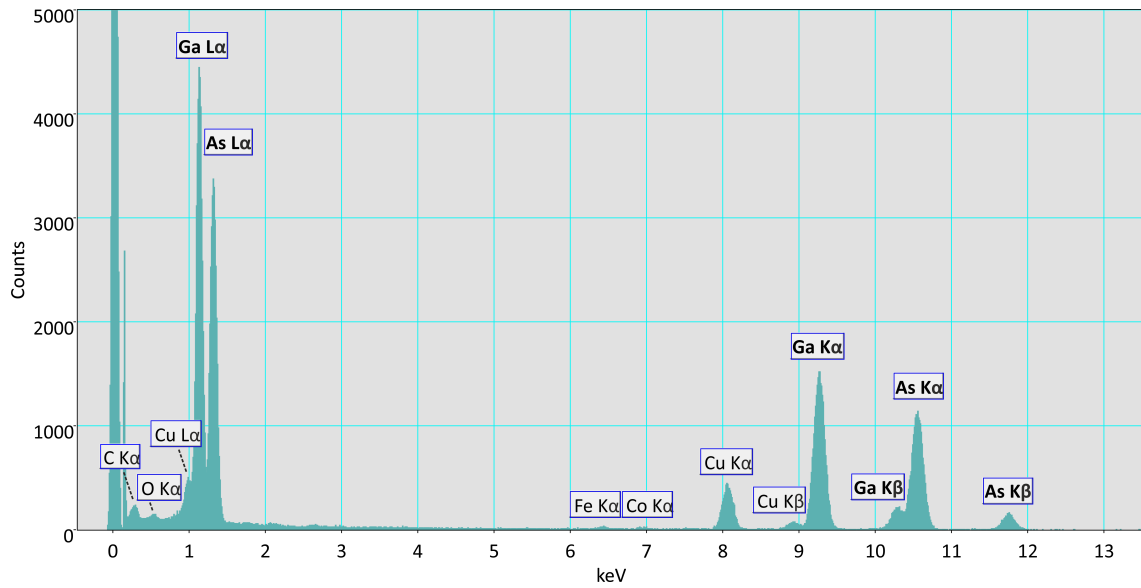


Figure 4.7: EDX spectrum of GaAs measured on the *Titan*³. Bold letters mark elements of the specimen. Other elements originate from the microscope, except of O and C due to contamination.

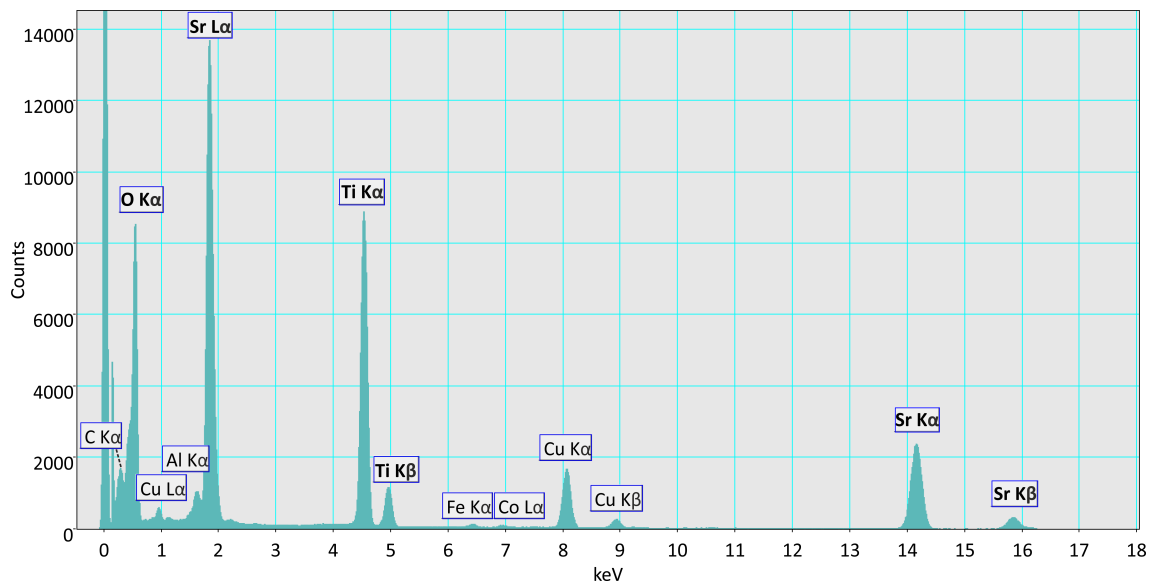


Figure 4.8: EDX spectrum of STO measured on the *Titan*³. Bold letters mark elements of the specimen. Other elements originate from the microscope, except of C (contamination).

Table 4.4: ζ -factors for K-lines of Ga, As, Ti and Sr measured with the EDX detectors quadrant I-IV of the Super-X system of the *Titan*³ and the Si(Li) detector of the *Tecnai F20*.

Element	ζ -factor [(kg · electron)/(m ² · photon)]				
	Super-X Q1	Super-X Q2	Super-X Q3	Super-X Q4	Si(Li)
Ti	756 ± 22	819 ± 9	780 ± 9	685 ± 2	2457 ± 56
Ga	1064 ± 57	1208 ± 9	1182 ± 34	1033 ± 22	3459 ± 52
As	1431 ± 81	1700 ± 76	1587 ± 60	1385 ± 20	4078 ± 94
Sr	2977 ± 70	3179 ± 29	2890 ± 26	2547 ± 14	5796 ± 186

In order to have a broader set of measured ζ -factors for the Super-X system additional values were used for the calculation of the solid angle, which were measured by Kraxner [43] during her PhD thesis at the FELMI-ZFE. She evaluated ζ -factors of Al-K with pure aluminium and the compound Al₂O₃ for all four quadrants and of Si-K with a pure silicon crystal and SiO₂ only for quadrant II and IV. These values are listed in table 4.5.

Table 4.5: ζ -factors for K-lines of Al and Si each measured with the pure elements and compounds for the Super-X quadrants I to IV of the *Titan*³.

Element	Specimen	ζ -factor [kg·electron/m ² ·photon]			
		Super-X Q1	Super-X Q2	Super-X Q3	Super-X Q4
Al	pure Al	621 ± 81	514 ± 18	530 ± 8	595 ± 21
	Al ₂ O ₃	544 ± 34	580 ± 45	584 ± 65	441 ± 5
Si	pure Si	531 ± 28	-	-	550 ± 9
	SiO ₂	564 ± 105	-	-	548 ± 98

4.6 Solid Angle Determination

Solid angles can be calculated via equation 2.10 by means of the measured ζ -factors and theoretical values for ionization cross sections, fluorescence yields and relative line intensities which were taken from the databases *NIST 164*, *EADL* and *MA-Table* (see chapter 3). Data for atomic weights originating from Wieser et al. [72] were used and detector efficiencies were derived with equation 2.2 and are listed in Table 4.6.

The results for the solid angles of the four Super-X quadrants and the Si(Li) detector are shown in Table 4.7. The values of every single element were averaged. Errors were determined via combined uncertainties in error propagation described in *Leitfaden zur Angabe der Unsicherheit beim Messen* [45].

Table 4.6: Detection efficiencies of the used SDD and Si(Li) detectors for the K_α lines of the listed elements.

	detection efficiency ε_A	
	SDD	Si(Li)
Al	0.9904	-
Si	0.9909	-
Ti	0.9879	0.7628
Ga	0.9879	0.7737
As	0.9516	0.7866
Sr	0.7193	0.8477

Table 4.7: Calculated solid angles via ζ -factors for the four Super-X quadrants and the Si(Li) detector. The arithmetic average is given in the last row.

Element	solid angle [sr]				
	Super-X Q1	Super-X Q2	Super-X Q3	Super-X Q4	Si(Li)
Al	0.14 ± 0.03	0.16 ± 0.03	0.16 ± 0.03	0.14 ± 0.03	-
	0.15 ± 0.03	0.15 ± 0.03	0.14 ± 0.03	0.19 ± 0.04	-
Si	0.15 ± 0.03	-	-	0.15 ± 0.03	-
	0.15 ± 0.04	-	-	0.15 ± 0.04	-
Ti	0.16 ± 0.03	0.15 ± 0.03	0.16 ± 0.03	0.18 ± 0.04	0.06 ± 0.01
Ga	0.15 ± 0.05	0.19 ± 0.04	0.17 ± 0.03	0.19 ± 0.04	0.06 ± 0.01
As	0.17 ± 0.03	0.14 ± 0.03	0.15 ± 0.03	0.17 ± 0.03	0.06 ± 0.01
Sr	0.15 ± 0.03	0.14 ± 0.03	0.16 ± 0.03	0.18 ± 0.04	0.06 ± 0.01
Av.	0.16 ± 0.01	0.15 ± 0.01	0.16 ± 0.01	0.17 ± 0.01	0.06 ± 0.01

To analyze the quality of the results, the received solid angles were compared to geometrically derived values. Kraxner [43] developed a geometrical simulation of the Super-X system, from which distances between the four detectors and the specimen as well as elevation angles were obtained. To compute the solid angle we used a formula employing elliptic integrals [20]. The outcome of this analytical solution is represented in Table 4.8. A comparison shows that the experimental and analytical values agree with each other.

Table 4.8: Analytically derived solid angles for the Super-X detector system. A ... Detector area d ... Distance between detector and specimen θ_e ... Elevation angle Ω_a ... Analytical solid angle $\Delta\Omega_a$... Deviation from experimental results

	Super-X Q1	Super-X Q2	Super-X Q3	Super-X Q4
A [mm ²]	30	30	30	30
d [mm]	13.4	13.3	13.8	12.5
θ_e [°]	16.5	15.8	19.0	19.6
Ω_a [sr]	0.157	0.160	0.147	0.179
$\Delta\Omega_a$ [%]	0%	+6%	-5%	+6%

CHAPTER 5

Conclusion

The object of this master thesis was the experimental determination of the solid angles of the Super-X detector on the *Titan*³ and the Si(Li) detector on the *Tecnai F20*. According to the theoretical definition of the ζ -factor, it is indirectly proportional to the solid angle. To obtain the solid angle via this relation, values for ζ -factors as well as data for the other occurring parameters are inevitable. Therefore ζ -factors for six elements (Al, Si, Ti, Ga, As, Sr) were measured with EDXS and theoretical data for ionization cross sections, fluorescence yields and relative line intensity ratios was gathered from literature and database research.

The literature research (see chapter 3) for values of ionization cross section, fluorescence yield and relative line intensity ratio revealed that full sets of databases concerning different energies and/or atomic number were more likely to be found for theoretically or semi empirically determined data. A general tendency or recommendation for specific theoretical or experimental data could be made; it was up to the scientist to choose reliable data.

All chosen values originated from complete (for energy and atomic number) and consistent sets of data. A profound uncertainty analysis to all data was an essential criteria in this case. Values for the relative line intensity ratios were taken from the software *MA-Table*, which was published in its newest version in 2015. Relative line intensity ratios originated from theoretical data published by Scofield [61, 62, 64, 65] and were corrected by experimental data from Afmann et al. [2] and Wendt [71] for selected values from outer shells. Data for fluorescence yields came from the database EADL published in 1991, which consisted of theoretically determined values. This database was recommended by the NIST. Ionization cross sections were taken from the database *NIST 164* published in 2014. An excessive uncertainty analysis and validation pointed out the quality of the database.

ζ -factors were measured by using two different reference specimens, namely GaAs and strontium titanate (SrTiO₃, STO). Their composition and density was known. Lamellas as well as needles were prepared with the FIB. X-ray intensities were measured with EDXS, whereas the thickness of the lamella in the case of GaAs was acquired via EELS

spectra and t/λ measurements. The inelastic mean free path λ was determined by t/λ measurements with the needle, where the thickness is known thanks to its rotationally symmetric geometry. In the case of STO only the needle was used for measurements. EDX spectra were acquired at the center along its vertical symmetry axis and its thickness was measured via HAADF images assuming that the width of the needle is equal to its thickness. Since channeling effects are highly amplified within zone axes, measuring outside of these axes was important.

Two further ζ -factors for Si and Ti, which had already been experimentally determined by Kraxner [43] were used for solid angle calculations.

Measured solid angles were compared to geometrical simulations of the four Super-X quadrants. It could be shown, that experimental and analytical values agree with each other.

Measurements of the solid angle at complete illumination reveal values for the four Super-X quadrants, that were a bit below the specifications of the manufacturer. We could show that the solid angle for each of the four detectors is between 0.15 to 0.17 sr, which is in total 0.63 ± 0.03 sr instead of 0.7 sr (given by FEI). A value of 0.06 ± 0.01 sr was measured for the solid angle of the Si(Li) detector of the *Tecnai F20*.

Bibliography

1. Asaad, W. N.: ‘Relativistic Calculation of the K-LL Auger Spectrum’. *Proceedings of the Royal Society A: Mathematical, Physical and Engineering Sciences* (1959), vol. 249(1259): pp. 555–573. ISSN: 1364-5021. DOI: [10.1098/rspa.1959.0045](https://doi.org/10.1098/rspa.1959.0045) (cit. on p. 17).
2. Aßmann, A. and M. Wendt: ‘The identification of soft X-ray lines’. *Spectrochimica Acta Part B: Atomic Spectroscopy* (2003), vol. 58(4): pp. 711–716. ISSN: 05848547. DOI: [10.1016/S0584-8547\(02\)00274-4](https://doi.org/10.1016/S0584-8547(02)00274-4) (cit. on pp. 16, 18, 45).
3. Bambynek, W., B. Crasemann, R. W. Fink, H. U. Freund, H. Mark, C. D. Swift, R. E. Price, and P. V. Rao: ‘X-Ray Fluorescence Yields, Auger, and Coster-Kronig Transition Probabilities’. *Reviews of Modern Physics* (1972), vol. 44(4): pp. 716–813. ISSN: 0034-6861. DOI: [10.1103/RevModPhys.44.716](https://doi.org/10.1103/RevModPhys.44.716) (cit. on pp. 15, 20).
4. Bearden, J. A.: ‘X-Ray Wavelengths’. *Reviews of Modern Physics* (1967), vol. 39(1): pp. 78–124. ISSN: 0034-6861. DOI: [10.1103/RevModPhys.39.78](https://doi.org/10.1103/RevModPhys.39.78) (cit. on p. 25).
5. Bethe, H.: ‘Zur Theorie des Durchgangs schneller Korpuskularstrahlen durch Materie’. *Annalen der Physik* (1930), vol. 397(3): pp. 325–400. ISSN: 00033804. DOI: [10.1002/andp.19303970303](https://doi.org/10.1002/andp.19303970303) (cit. on p. 23).
6. Bhalla, C. P.: ‘Radiative transition probabilities for vacancies in M sub-shells’. *Journal of Physics B: Atomic and Molecular Physics* (1970), vol. 3(7): pp. 916–924. ISSN: 0022-3700. DOI: [10.1088/0022-3700/3/7/004](https://doi.org/10.1088/0022-3700/3/7/004) (cit. on p. 16).
7. Bloch, S.: ‘Über die sekundäre Kathodenstrahlung in Gasen bei großer Primär-geschwindigkeit’. *Annalen der Physik* (1912), vol. 343(8): pp. 559–587. ISSN: 00033804 (cit. on p. 23).
8. Bote, D. and F. Salvat: ‘Calculations of inner-shell ionization by electron impact with the distorted-wave and plane-wave Born approximations’. *Physical Review A* (2008), vol. 77(4). ISSN: 1050-2947. DOI: [10.1103/PhysRevA.77.042701](https://doi.org/10.1103/PhysRevA.77.042701) (cit. on pp. 23–26).
9. Bote, D., F. Salvat, A. Jablonski, and C. J. Powell: ‘Cross sections for ionization of K, L and M shells of atoms by impact of electrons and positrons with energies up to 1GeV: Analytical formulas’. *Atomic Data and Nuclear Data Tables* (2009), vol. 95(6): pp. 871–909. ISSN: 0092640X. DOI: [10.1016/j.adt.2009.08.001](https://doi.org/10.1016/j.adt.2009.08.001) (cit. on pp. 23–26).

10. Bote, D., F. Salvat, A. Jablonski, and C. J. Powell: ‘Erratum to “Cross sections for ionization of K, L and M shells of atoms by impact of electrons and positrons with energies up to 1GeV. Analytical formulas” [At. Data Nucl. Data Tables 95 (2009) 871–909]’. *Atomic Data and Nuclear Data Tables* (2011), vol. 97(2): p. 186. ISSN: 0092640X. DOI: [10.1016/j.adt.2010.10.001](https://doi.org/10.1016/j.adt.2010.10.001) (cit. on p. 25).
11. Carlson, T. A.: *Photoelectron and Auger Spectroscopy*. New York: Plenum Press, 1975 (cit. on p. 25).
12. Casnati, E., A. Tartari, and C. Baraldi: ‘An empirical approach to K-shell ionisation cross section by electrons’. *Journal of Physics B: Atomic and Molecular Physics* (1982), vol. 15(1): pp. 155–167. ISSN: 0022-3700. DOI: [10.1088/0022-3700/15/1/022](https://doi.org/10.1088/0022-3700/15/1/022) (cit. on p. 23).
13. Chen, M. H. and B. Crasemann: ‘M x-ray emission rates in Dirac-Fock approximation’. *Physical Review A* (1984), vol. 30(1): pp. 170–176. ISSN: 1050-2947. DOI: [10.1103/PhysRevA.30.170](https://doi.org/10.1103/PhysRevA.30.170) (cit. on p. 16).
14. Chen, M. H., B. Crasemann, and H. Mark: ‘Relativistic radiationless transition probabilities for atomic K- and L-shells’. *Atomic Data and Nuclear Data Tables* (1979), vol. 24(1): pp. 13–37. ISSN: 0092640X. DOI: [10.1016/0092-640X\(79\)90037-8](https://doi.org/10.1016/0092-640X(79)90037-8) (cit. on pp. 21, 22).
15. Chen, M. H., B. Crasemann, and H. Mark: ‘Relativistic K -shell Auger rates, level widths, and fluorescence yields’. *Physical Review A* (1980), vol. 21(2): pp. 436–441. ISSN: 1050-2947. DOI: [10.1103/PhysRevA.21.436](https://doi.org/10.1103/PhysRevA.21.436) (cit. on pp. 21, 22).
16. Chen, M. H., B. Crasemann, and H. Mark: ‘Widths and fluorescence yields of atomic L -shell vacancy states’. *Physical Review A* (1981), vol. 24(1): pp. 177–182. ISSN: 1050-2947. DOI: [10.1103/PhysRevA.24.177](https://doi.org/10.1103/PhysRevA.24.177) (cit. on pp. 21, 22).
17. Chen, M. H., B. Crasemann, and H. Mark: ‘Radiationless transitions to atomic M_{1,2,3} shells: Results of relativistic theory’. *Physical Review A* (1983), vol. 27(6): pp. 2989–2994. ISSN: 1050-2947. DOI: [10.1103/PhysRevA.27.2989](https://doi.org/10.1103/PhysRevA.27.2989) (cit. on pp. 21, 22).
18. Chen, M. H., E. Laiman, B. Crasemann, M. Aoyagi, and H. Mark: ‘Relativistic L -shell Auger and Coster-Kronig rates and fluorescence yields’. *Physical Review A* (1979), vol. 19(6): pp. 2253–2259. ISSN: 1050-2947. DOI: [10.1103/PhysRevA.19.2253](https://doi.org/10.1103/PhysRevA.19.2253) (cit. on pp. 21, 22).
19. Cliff, G. and G. W. Lorimer: ‘The quantitative analysis of thin specimens’. *Journal of Microscopy* (1975), vol. 103(2): pp. 203–207. DOI: [10.1111/j.1365-2818.1975.tb03895.x](https://doi.org/10.1111/j.1365-2818.1975.tb03895.x) (cit. on p. 13).
20. Conway, J. T.: ‘Analytical solution for the solid angle subtended at any point by an ellipse via a point source radiation vector potential’. *Nuclear Instruments and Methods in Physics Research Section A: Accelerators, Spectrometers, Detectors and Associated Equipment* (2010), vol. 614(1): pp. 17–27. ISSN: 01689002. DOI: [10.1016/j.nima.2009.11.075](https://doi.org/10.1016/j.nima.2009.11.075) (cit. on pp. 11, 43).

21. Deslattes, R. D., E. G. Kessler, P. Indelicato, L. de Billy, E. Lindroth, and J. Anton: ‘X-ray transition energies: new approach to a comprehensive evaluation’. *Reviews of Modern Physics* (2003), vol. 75(1): pp. 35–99. ISSN: 0034-6861. DOI: [10.1103/RevModPhys.75.35](https://doi.org/10.1103/RevModPhys.75.35) (cit. on p. 25).
22. Dolder, K. T., Harrison, M. F. A., and P. C. Thonemann: ‘A Measurement of the Ionization Cross-Section of Helium Ions by Electron Impact’. *Proceedings of the Royal Society A: Mathematical, Physical and Engineering Sciences* (1961), vol. 264(1318): pp. 367–378. ISSN: 1364-5021. DOI: [10.1098/rspa.1961.0205](https://doi.org/10.1098/rspa.1961.0205) (cit. on p. 23).
23. Egerton, R. F.: *Electron energy-loss spectroscopy in the electron microscope*. 3rd ed. The language of science. New York: Springer, 2011. ISBN: 978-1-4419-9582-7 (cit. on p. 37).
24. Egerton, R. F. and S. C. Cheng: ‘Characterization of an analytical electron microscope with a NiO test specimen’. *Ultramicroscopy* (1994), vol. 55(1): pp. 43–54. DOI: [10.1016/0304-3991\(94\)90079-5](https://doi.org/10.1016/0304-3991(94)90079-5) (cit. on pp. 2, 12, 14, 15, 27, 28).
25. Eggert, F.: ‘EDX-Spectra Simulation in Electron Probe Microanalysis. Optimization of Excitation Conditions and Detection Limits’. *Microchimica Acta* (2006), vol. 155(1-2): pp. 129–136. ISSN: 0026-3672. DOI: [10.1007/s00604-006-0530-0](https://doi.org/10.1007/s00604-006-0530-0) (cit. on pp. 17, 18).
26. Eggert, F.: *MA-Table*. 2015. URL: <http://www.microanalyst.net> (cit. on pp. 16, 17).
27. Fladischer, S.: ‘Application of new EDXS quantification schemes in TEM to organic semiconducting devices’. PhD thesis. Graz: Graz University of Technology, 2013 (cit. on pp. 8, 9).
28. Gauvin, R.: ‘What remains to be done to allow quantitative X-ray microanalysis performed with EDS to become a true characterization technique?’ *Microscopy and microanalysis : the official journal of Microscopy Society of America, Microbeam Analysis Society, Microscopical Society of Canada* (2012), vol. 18(5): pp. 915–940. ISSN: 1435-8115. DOI: [10.1017/S1431927612001468](https://doi.org/10.1017/S1431927612001468) (cit. on p. 13).
29. Giannuzzi, L. A. and F. A. Stevie: *Introduction to focused ion beams: Instrumentation, theory, techniques, and practice*. New York: Springer, 2005. ISBN: 978-0-387-23116-7. DOI: [10.1007/b101190](https://doi.org/10.1007/b101190) (cit. on p. 30).
30. Haque, A K F, M. R. Talukder, M. Shahjahan, M. A. Uddin, A. K. Basak, and B. C. Saha: ‘An extended empirical formula for inner-shell ionization of atoms’. *Journal of Physics B: Atomic, Molecular and Optical Physics* (2010), vol. 43(11): p. 115201. DOI: [10.1088/0953-4075/43/11/115201](https://doi.org/10.1088/0953-4075/43/11/115201) (cit. on p. 23).
31. Haque, A. K. F., M. A. Uddin, A. K. Basak, K. R. Karim, and B. C. Saha: ‘Empirical model for the electron-impact K -shell-ionization cross sections’. *Physical Review A* (2006), vol. 73(1). ISSN: 1050-2947. DOI: [10.1103/PhysRevA.73.012708](https://doi.org/10.1103/PhysRevA.73.012708) (cit. on p. 23).

32. Harrach, S. von, P. Dona, B. Freitag, H. Soltau, A. Niculae, and M. Rohde: ‘An integrated Silicon Drift Detector System for FEI Schottky Field Emission Transmission Electron Microscopes’. *Microscopy and Microanalysis* (2009), vol. 15(S2): pp. 208–209. ISSN: 1431-9276. DOI: [10.1017/S1431927609094288](https://doi.org/10.1017/S1431927609094288) (cit. on p. 11).
33. Hombourger, C.: ‘An empirical expression for K-shell ionization cross section by electron impact’. *Journal of Physics B: Atomic, Molecular and Optical Physics* (1998), vol. 31(16): pp. 3693–3702. DOI: [10.1088/0953-4075/31/16/020](https://doi.org/10.1088/0953-4075/31/16/020) (cit. on p. 23).
34. Howerton, R. J., R. E. Dye, P. C. Giles, J. R. Kimlinger, S. T. Perkins, and E. F. Plechaty: *OMEGA: a Cray 1 executive code for LLNL nuclear data libraries: UCRL-50400 Vol. 25*. Ed. by Lawrence Livermore National Laboratory. Livermore, CA, USA, 1983 (cit. on p. 20).
35. Hubbell, J. H.: *Bibliography and Current Status of K, L, and Higher Shell Fluorescence Yields for Computations of Photon Energy-Absorption Coefficients: NISTIR 89-4144*. Ed. by National Institute of Standards and Technology. Gaithersburg, 1989 (cit. on p. 21).
36. Hubbell, J. H., P. N. Trehan, Nirmal Singh, B. Chand, D. Mehta, M. L. Garg, R. R. Garg, Surinder Singh, and S. Puri: ‘A Review, Bibliography, and Tabulation of K, L, and Higher Atomic Shell X-Ray Fluorescence Yields’. *Journal of Physical and Chemical Reference Data* (1994), vol. 23(2): p. 339. ISSN: 0047-2689. DOI: [10.1063/1.555955](https://doi.org/10.1063/1.555955) (cit. on p. 20).
37. Kim, Y.-K. and M. E. Rudd: ‘Binary-encounter-dipole model for electron-impact ionization’. *Physical Review A* (1994), vol. 50(5): pp. 3954–3967. ISSN: 1050-2947. DOI: [10.1103/PhysRevA.50.3954](https://doi.org/10.1103/PhysRevA.50.3954) (cit. on p. 23).
38. Kim, Y.-K., J. P. Santos, and F. Parente: ‘Extension of the binary-encounter-dipole model to relativistic incident electrons’. *Physical Review A* (2000), vol. 62(5). ISSN: 1050-2947. DOI: [10.1103/PhysRevA.62.052710](https://doi.org/10.1103/PhysRevA.62.052710) (cit. on p. 23).
39. Kolbenstvedt, H.: ‘Simple Theory for K-Ionization by Relativistic Electrons’. *Journal of Applied Physics* (1967), vol. 38(12): p. 4785. DOI: [10.1063/1.1709220](https://doi.org/10.1063/1.1709220) (cit. on p. 23).
40. Kotula, P. G., J. R. Michael, and M. Rohde: ‘Results from Two Four-Channel Si-drift Detectors on an SEM: Conventional and Annular Geometries’. *Microscopy and Microanalysis* (2008), vol. 14(S2): pp. 116–117. ISSN: 1431-9276. DOI: [10.1017/S1431927608081701](https://doi.org/10.1017/S1431927608081701) (cit. on p. 11).
41. Kramers, H. A.: ‘On the theory of X-ray absorption and of the continuous X-ray spectrum’. *Philosophical Magazine Series 6* (1923), vol. 46(275): pp. 836–871. ISSN: 1941-5982. DOI: [10.1080/14786442308565244](https://doi.org/10.1080/14786442308565244) (cit. on p. 3).
42. Krause, M. O.: ‘Atomic radiative and radiationless yields for K and L shells’. *Journal of Physical and Chemical Reference Data* (1979), vol. 8(2): p. 307. ISSN: 0047-2689. DOI: [10.1063/1.555594](https://doi.org/10.1063/1.555594) (cit. on p. 20).
43. Kraxner, J.: ‘PhD thesis still in progress and will be pulished in spring 2016’. PhD thesis. Technische Universität Graz, 2016 (cit. on pp. 29, 42, 43, 46).

44. Lechner, P., S. Eckbauer, R. Hartmann, S. Krisch, D. Hauff, R. Richter, H. Soltau, L. Strüder, C. Fiorini, E. Gatti, A. Longoni, and M. Sampietro: ‘Silicon drift detectors for high resolution room temperature X-ray spectroscopy’. *Nuclear Instruments and Methods in Physics Research Section A: Accelerators, Spectrometers, Detectors and Associated Equipment* (1996), vol. 377(2-3): pp. 346–351. ISSN: 01689002. DOI: [10.1016/0168-9002\(96\)00210-0](https://doi.org/10.1016/0168-9002(96)00210-0) (cit. on p. 7).
45. *Leitfaden zur Angabe der Unsicherheit beim Messen*. 1. Aufl. Berlin [u.a.]: Beuth, 1995. ISBN: 3-410-13405-0 (cit. on p. 42).
46. Lenard, P.: ‘Über Kathodenstrahlen in Gasen von atmosphärischem Druck und im äußersten Vacuum’. *Annalen der Physik und Chemie* (1894), vol. 51: pp. 225–267 (cit. on p. 23).
47. Lide D. R., ed.: *CRC Handbook of Chemistry and Physics, Internet Version 2005*. Boca Raton, FL, 2005. URL: <http://www.hbcpnetbase.com> (cit. on p. 39).
48. Liu, M., Z. An, C. Tang, Z. Luo, X. Peng, and X. Long: ‘Experimental Electron-Impact K-Shell Ionization Cross Sections’. *Atomic Data and Nuclear Data Tables* (2000), vol. 76(2): pp. 213–234. ISSN: 0092640X. DOI: [10.1006/adnd.2000.0843](https://doi.org/10.1006/adnd.2000.0843) (cit. on p. 23).
49. Llovet, X., C. J. Powell, F. Salvat, and A. Jablonski: ‘Cross Sections for Inner-Shell Ionization by Electron Impact’. *Journal of Physical and Chemical Reference Data* (2014), vol. 43(1): p. 013102. ISSN: 0047-2689. DOI: [10.1063/1.4832851](https://doi.org/10.1063/1.4832851) (cit. on pp. 23, 24, 26, 27).
50. Llovet, X., F. Salvat, D. Bote, F. Salvat-Pujol, Jablonski A., and C. J. Powell: *NIST database of cross sections for inner-shell ionization by electron or positron impact: Version 1.0 user’s guide*. National Institute of Standards and Technology, 2014. DOI: [10.6028/NIST.NSRDS.164](https://doi.org/10.6028/NIST.NSRDS.164) (cit. on pp. 23, 25).
51. Lotz, W.: ‘Electron-impact ionization cross-sections for atoms up to Z=108’. *Z. Physik (Zeitschrift fuer Physik)* (1970), vol. 232(2): pp. 101–107. DOI: [10.1007/BF01393132](https://doi.org/10.1007/BF01393132) (cit. on p. 23).
52. Perkins, S. T., D. E. Cullen, M. H. Chen, J. H. Hubbell, J. Rathkopf, and J. Scofield: *Tables and Graphs of Atomic Subshell and Relaxation Data Derived from the LLNL Evaluated Atomic Data Library (EADL), Z = 1 - 100: UCRL-50400 Vol. 30*. Ed. by Lawrence Livermore National Laboratory. Livermore, CA, USA, October 31, 1991 (cit. on pp. 20–22, 25).
53. Pia, M. G., P. Saracco, and M. Sudhakar: ‘Validation of K and L Shell Radiative Transition Probability Calculations’. *IEEE Transactions on Nuclear Science* (2009), vol. 56(6): pp. 3650–3661. DOI: [10.1109/TNS.2009.2033793](https://doi.org/10.1109/TNS.2009.2033793) (cit. on p. 18).
54. Powell, C. J.: ‘Cross sections for ionization of inner-shell electrons by electrons’. *Reviews of Modern Physics* (1976), vol. 48(1): pp. 33–47. ISSN: 0034-6861. DOI: [10.1103/RevModPhys.48.33](https://doi.org/10.1103/RevModPhys.48.33) (cit. on p. 23).
55. Powell, C. J.: ‘Innershell Ionization Cross Sections’. *Electron impact ionization*. Ed. by Märk, T. D. and G. H. Dunn. Wien and New York: Springer-Verlag, 1985: pp. 198–231. ISBN: 978-3-7091-4030-7 (cit. on p. 23).

56. Ritchie, Nicholas: *private communication: E-Mail*. Ed. by Lammer, Judith. 5.06.2015 (cit. on p. 20).
57. Salem, S. I., S. L. Panossian, and R. A. Krause: ‘Experimental K and L relative x-ray emission rates’. *Atomic Data and Nuclear Data Tables* (1974), vol. 14(2): pp. 91–109. ISSN: 0092640X. DOI: [10.1016/S0092-640X\(74\)80017-3](https://doi.org/10.1016/S0092-640X(74)80017-3) (cit. on p. 16).
58. Santos, J. P., F. Parente, and Y.-K. Kim: ‘Cross sections for K-shell ionization of atoms by electron impact’. *Journal of Physics B: Atomic, Molecular and Optical Physics* (2003), vol. 36(21): pp. 4211–4224. DOI: [10.1088/0953-4075/36/21/002](https://doi.org/10.1088/0953-4075/36/21/002) (cit. on p. 23).
59. Schlossmacher, P., D. O. Klenov, B. Freitag, S. von Harrach, and A. Steinbach: ‘Nanoscale Chemical Compositional Analysis with an Innovative S/TEM-EDX System’. *Microscopy and Analysis* (2010), vol. 24(7): pp. 5–8 (cit. on p. 31).
60. Schreiber, T. P. and A. M. Wims: ‘Relative intensity factors for K, L and M shell x-ray lines’. *X-Ray Spectrometry* (1982), vol. 11(2): pp. 42–45. DOI: [10.1002/xrs.1300110203](https://doi.org/10.1002/xrs.1300110203) (cit. on p. 16).
61. Scofield, J. H.: ‘Radiative Decay Rates of Vacancies in the K and L Shells’. *Physical Review* (1969), vol. 179(1): pp. 9–16. ISSN: 0031-899X. DOI: [10.1103/PhysRev.179.9](https://doi.org/10.1103/PhysRev.179.9) (cit. on pp. 16–18, 21, 22, 45).
62. Scofield, J. H.: ‘Exchange corrections of K x-ray emission rates’. *Physical Review A* (1974), vol. 9(3): pp. 1041–1049. ISSN: 1050-2947. DOI: [10.1103/PhysRevA.9.1041](https://doi.org/10.1103/PhysRevA.9.1041) (cit. on pp. 16, 17, 45).
63. Scofield, J. H.: ‘Hartree-Fock values of L x-ray emission rates’. *Physical Review A* (1974), vol. 10(5): pp. 1507–1510. ISSN: 1050-2947. DOI: [10.1103/PhysRevA.10.1507](https://doi.org/10.1103/PhysRevA.10.1507) (cit. on p. 17).
64. Scofield, J. H.: ‘Relativistic hartree-slater values for K and L X-ray emission rates’. *Atomic Data and Nuclear Data Tables* (1974), vol. 14(2): pp. 121–137. ISSN: 0092640X. DOI: [10.1016/S0092-640X\(74\)80019-7](https://doi.org/10.1016/S0092-640X(74)80019-7) (cit. on pp. 16–18, 21, 22, 45).
65. Scofield, J. H.: ‘Radiative Transitions’. *Ionization and transition probabilities*. Ed. by Crasemann, B. Vol. 1. Atomic inner-shell processes. New York [u.a]: Acad. Press, 1975: p. 265. ISBN: 0-12-196901-0(v.1) (cit. on pp. 16–18, 21, 22, 45).
66. Scofield, J. H.: ‘K - and L -shell ionization of atoms by relativistic electrons’. *Physical Review A* (1978), vol. 18(3): pp. 963–970. ISSN: 1050-2947. DOI: [10.1103/PhysRevA.18.963](https://doi.org/10.1103/PhysRevA.18.963) (cit. on p. 23).
67. Scofield, J. H.: *Theoretical photoionization cross sections from 1 to 1500 keV: UCRL-51326*. Livermore, CA, USA, January 01, 1973. DOI: [10.2172/4545040](https://doi.org/10.2172/4545040) (cit. on p. 25).
68. Thomson, J. J.: ‘Ionization by moving electrified particles’. *Philosophical Magazine Series 6* (1912), vol. 23(136): pp. 449–457. ISSN: 1941-5982. DOI: [10.1080/14786440408637241](https://doi.org/10.1080/14786440408637241) (cit. on p. 23).

69. Watanabe, M.: 'X-Ray Energy-Dispersive Spectrometry in Scanning Transmission Electron Microscopes'. *Scanning transmission electron microscopy*. Ed. by Pennycook, S. J. and P. D. Nellist. New York: Springer, 2011: pp. 291–351. ISBN: 978-1-4419-7199-9 (cit. on p. 11).
70. Watanabe, M. and D. B. Williams: 'The quantitative analysis of thin specimens: a review of progress from the Cliff-Lorimer to the new zeta-factor methods'. *Journal of Microscopy* (2006), vol. 221(Pt 2): pp. 89–109. DOI: [10.1111/j.1365-2818.2006.01549.x](https://doi.org/10.1111/j.1365-2818.2006.01549.x) (cit. on pp. 13–15).
71. Wendt, M.: 'M Spectra of Elements $39 \leq Z \leq 56$ Measured with an Ultra-Thin Window Si(Li) Detector'. *Microchimica Acta* (2002), vol. 139(1-4): pp. 195–200. ISSN: 0026-3672. DOI: [10.1007/s006040200061](https://doi.org/10.1007/s006040200061) (cit. on pp. 16, 18, 45).
72. Wieser, M. E. et al.: 'Atomic weights of the elements 2011 (IUPAC Technical Report)'. *Pure and Applied Chemistry* (2013), vol. 85(5): pp. 1047–1078. ISSN: 1365-3075. DOI: [10.1351/PAC-REP-13-03-02](https://doi.org/10.1351/PAC-REP-13-03-02) (cit. on p. 42).
73. Williams, D. B. and C. B. Carter: *Transmission electron microscopy: A textbook for materials science*. 2nd ed. New York: Springer, 2009. ISBN: 978-0-387-76500-6 (cit. on pp. 4–8, 10).
74. Williams, E. J.: 'Applications of the Method of Impact Parameter in Collisions'. *Proceedings of the Royal Society A: Mathematical, Physical and Engineering Sciences* (1933), vol. 139(837): pp. 163–186. ISSN: 1364-5021. DOI: [10.1098/rspa.1933.0012](https://doi.org/10.1098/rspa.1933.0012) (cit. on p. 23).
75. Williams and G. P.: 'Electron Binding Energies of the Elements: Section 10'. *CRC Handbook of Chemistry and Physics, Internet Version 2005*. Ed. by Lide D. R. Boca Raton, FL, 2005: p. 200 (cit. on p. 25).
76. Zaluzec, N. J.: 'Detector solid angle formulas for use in X-ray energy dispersive spectrometry'. *Microscopy and microanalysis : the official journal of Microscopy Society of America, Microbeam Analysis Society, Microscopical Society of Canada* (2009), vol. 15(2): pp. 93–98. ISSN: 1435-8115. DOI: [10.1017/S1431927609090217](https://doi.org/10.1017/S1431927609090217) (cit. on p. 11).
77. Zaluzec, N. J.: 'Innovative Instrumentation for Analysis of Nanoparticles: The π Steradian Detector'. *Microscopy Today* (2009), vol. 17(04): p. 56. ISSN: 1551-9295. DOI: [10.1017/S1551929509000224](https://doi.org/10.1017/S1551929509000224) (cit. on p. 11).
78. Zaluzec, N. J.: 'Analytical formulae for calculation of X-ray detector solid angles in the scanning and scanning/transmission analytical electron microscope'. *Microscopy and microanalysis : the official journal of Microscopy Society of America, Microbeam Analysis Society, Microscopical Society of Canada* (2014), vol. 20(4): pp. 1318–1326. ISSN: 1435-8115. DOI: [10.1017/S1431927614000956](https://doi.org/10.1017/S1431927614000956) (cit. on pp. 10, 11).
79. Zschornack, G.: *Handbook of X-ray data*. New York: Springer, 2006. ISBN: 978-3-540-28618-9 (cit. on pp. 16, 19, 20).

80. Zulliger, H. R. and D. W. Aitken: 'Fano Factor Fact and Fallacy'. *IEEE Transactions on Nuclear Science* (1970), vol. 17(3): pp. 187–195. DOI: [10.1109/TNS.1970.4325691](https://doi.org/10.1109/TNS.1970.4325691) (cit. on p. 7).